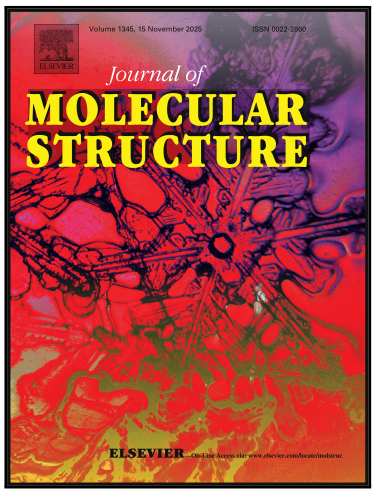
Journal Pre-proof



Two-Dimensional Copper (II) Coordination Polymer with Antimicrobial and DNA-Cleavage Activity

Maryam Aghaee , Khosro Mohammadi , Payam Hayati , Jan Janczak , Constantinos D. Zeinalipour-Yazdi , Reza Naghiha

PII: S0022-2860(26)02076-4
DOI: https://doi.org/10.1016/j.molstruc.2026.147322
Reference: MOLSTR 147322

To appear in: *Journal of Molecular Structure*

Received date: 14 June 2026
Revised date: 25 July 2026
Accepted date: 9 August 2026

Please cite this article as: Maryam Aghaee , Khosro Mohammadi , Payam Hayati , Jan Janczak , Constantinos D. Zeinalipour-Yazdi , Reza Naghiha , Two-Dimensional Copper (II) Coordination Polymer with Antimicrobial and DNA-Cleavage Activity, *Journal of Molecular Structure* (2026), doi: https://doi.org/10.1016/j.molstruc.2026.147322

This is a PDF of an article that has undergone enhancements after acceptance, such as the addition of a cover page and metadata, and formatting for readability. This version will undergo additional copyediting, typesetting and review before it is published in its final form. As such, this version is no longer the Accepted Manuscript, but it is not yet the definitive Version of Record; we are providing this early version to give early visibility of the article. Please note that Elsevier's sharing policy for the Published Journal Article applies to this version, see: https://www.elsevier.com/about/policies-and-standards/sharing#4-published-journal-article. Please also note that, during the production process, errors may be discovered which could affect the content, and all legal disclaimers that apply to the journal pertain.

© 2026 Published by Elsevier B.V.

Journal Pre-proof

Highlights

- A new 2D copper(II) coordination polymer, $[Cu(\mu\text{-}L)(\kappa^2\text{-}L')(\mu\text{-}L')_2(H_2O)]_n$ (**1**) (which are employing L = 4,4'-bipyridine and HL′ = 4-carboxybenzaldehyde),was synthesized and structurally characterized, revealing a six-coordinate Cu(II) center.
- The polymer exhibited notable antimicrobial activity against both Gram-negative (*E. coli* and *P. aeruginosa*) and Gram-positive (*B. subtilis* and *S. aureus*) bacteria, along with effective DNA cleavage capability.
- Complementary molecular orbital analyses were performed to elucidate the binding interactions underlying the observed biological activity.

Journal Pre-proof

Journal Pre-proof

Two-Dimensional Copper (II) Coordination Polymer with Antimicrobial and DNA-Cleavage Activity

Maryam Aghaee[a], Khosro Mohammadi[*a], Payam Hayati[**b], Jan Janczak[c], Constantinos D. Zeinalipour-Yazdi[d], Reza Naghiha[e]

[a] *Chemistry Department, Faculty of Nano and Bio Science and Technology, Persian Gulf University, Bushehr 75169, Iran*

[b] *Department of Applied Chemistry, Faculty of Gas and Petroleum, Yasouj University, P. O. Box 353, Gachsaran, 75918-74831, Iran*

[c] *Institute of Low Temperature and Structure Research, Polish Academy of Sciences, P. O. Box 1410, Okolna 2 str., 50-950 Wroclaw, Poland*

[d] *Biosciences and Chemistry, Faculty of Computing, Mathematics, Engineering and Natural Sciences, Northeastern University London, 1 Portsoken Street, E1 8BT, London, UK*

[e] *Department of Pathobiology, Faculty of Veterinary Medicine, Shahid Chamran University of Ahvaz, Ahvaz, Iran*

Corresponding Authors: *Email: khmohammadi@pgu.ac.ir, khmohammadi@yahoo.com;, ** Email: payam.hayati@uninsubria.it, payamhayati@yahoo.com

Journal Pre-proof

Abstract

A new two-dimensional copper(II) coordination polymer, $[Cu(\mu\text{-}L)(\kappa^2\text{-}L')(\mu\text{-}L')_2(H_2O)]_n$ (**1**), utilizing 4,4'-bipyridine (L) and 4-carboxybenzaldehyde (HL′) as ligands, was synthesized as both bulk single-crystalline material and submicro-structured form (compound **1′**) via an ultrasound-assisted method. Single-crystal X-ray diffraction analysis unequivocally established the polymeric framework and confirmed that the Cu(II) centers adopt a distorted octahedral coordination geometry. Complementary techniques, including powder X-ray diffraction, FTIR spectroscopy,

scanning electron microscopy, and thermogravimetric analysis, provided supporting evidence for phase purity, coordination modes, morphological features, and thermal stability of the synthesized materials. Hirshfeld surface and fingerprint plot analyses were employed to investigate the intermolecular contacts governing the supramolecular packing architecture. Ultrasound irradiation produced plate-like submicro-structured particles with a relatively narrow size distribution, as observed by SEM (127–150 nm for primary particles). DLS analysis further revealed a mean hydrodynamic diameter of approximately 490 nm, indicating the formation of stable aggregates in aqueous media. The in vitro biological evaluation of compound (**1′**) revealed that the material exhibits DNA cleavage activity under oxidative conditions, as demonstrated by agarose gel electrophoresis experiments, indicating notable nuclease-like behavior. Antimicrobial assays showed a concentration-dependent inhibitory effect against both Gram-positive and Gram-negative bacteria, although the activity remained lower than that of standard reference antibiotics. These findings suggest that the biological response of compound (**1′**) is influenced by both the distorted Cu(II) coordination environment and the supramolecular features of the framework. Collectively, the structural and biological results position compound (**1**) and its submicro-structured form (**1′**) as coordination materials warranting further investigation in supramolecular and bioinorganic chemistry.

Journal Pre-proof

Keywords: Metal organic coordination polymer; Ultrasound irradiation; 4,4'-Bipyridine; 4-Carboxybenzaldehyde; Morphology; Antimicrobial; DNA cleavage

1. Introduction

Metal-Organic Coordination Polymers (MOCPs) represent a distinct category of crystalline hybrid systems that originate from the self-assembly of metal centers with organic bridging ligands, thus providing exceptional structural variety and chemical adaptability [1,2]. Their inherent backbone flexibility allows for the deliberate adjustment of physicochemical characteristics, which positions them as promising platforms for deployment in heterogeneous catalysis, chemical sensing, and therapeutic interventions [3–9]. From the broad spectrum of transition metals currently explored, copper(II) has attracted particular attention owing to its diverse coordination preferences, prominent redox chemistry, and thoroughly documented biological profile, which encompasses antibacterial, antifungal, and anticancer activities [10–12].

The biological action of copper(II) centers proceeds through several concurrent pathways, including the initiation of reactive oxygen species (ROS) production via Fenton-like redox cycling, the establishment of electrostatic contacts with microbial membrane surfaces, and the sustained leaching of Cu^{2+} species from the coordination architecture [13]. When compared with standard antibiotic agents, Cu(II)-based coordination networks exhibit remarkable benefits, among which are their multitargeted mechanisms, structural fine-tunability, and pronounced competence in counteracting drug-resistant microbial strains [14,15]. Recent findings have disclosed the utility of copper-containing compounds in a wide array of biomedical contexts, ranging from the suppression of biofilm development to the facilitation of cutaneous wound repair, thereby reflecting the escalating research enthusiasm directed toward their biological translation [13,16].

The fabrication of MOCPs may proceed through several well-established routes, comprising hydrothermal treatment, solution-phase diffusion, and sequential layer-by-layer deposition strategies. Within this methodological repertoire, ultrasonically mediated synthesis has gained

widespread recognition as a particularly productive strategy, conferring distinct operational benefits such as shortened reaction intervals, milder thermal conditions, and superior regulation over crystallite geometry and particle size homogeneity [17,18]. The underlying physical principle acoustic cavitation, which induces transient localized zones of extreme energy acts to accelerate both the primary nucleation events and the subsequent crystalline growth stages, thereby establishing sonochemistry as a powerful and adaptable technique for the production of MOCPs with precisely tailored micro and submicro-scale morphological features [19–31].

Notwithstanding the considerable body of crystallographic investigations devoted to Cu(II) coordination compounds, relatively few systematic efforts have addressed the critical issue of how coordination environment, supramolecular packing arrangement, and external crystalline morphology contribute to the resulting bioactivity profiles [32–38]. A comprehensive elucidation of these structure–activity relationships (SAR) is of fundamental importance for the informed and rational construction of next-generation antimicrobial materials.

In this connection, the present work describes the preparation and full characterization of a novel two-dimensional Cu(II) coordination polymer, formulated as $[Cu(\mu\text{-}L)(\kappa^2\text{-}L')(\mu\text{-}L')_2(H_2O)]_n$ (**1**) (wherein L denotes 4,4'-bipyridine and HL′ corresponds to 4-carboxybenzaldehyde), which has been isolated both as bulk single crystals and as submicro-structured particulates (designated **1′**) through the application of an ultrasonically assisted synthetic protocol. The deliberate choice of 4,4'-bipyridine as a rigid N,N-donor bridging unit, alongside 4-carboxybenzaldehyde as a complementary O-donor co-ligand, rests upon their well-established capacity to generate robust coordination networks further stabilized by supplementary π–π stacking contacts and directional hydrogen-bonding interactions [39]. A systematic investigation of the structural, supramolecular, and morphological characteristics of both (**1**) and (**1′**) has been undertaken, with particular

emphasis placed on establishing meaningful correlations between these physicochemical attributes and the observed DNA cleavage efficiency as well as antimicrobial potency.

2. Experimental

2.1. Materials

All the chemicals and solvents were purchased from Sigma-Aldrich, Merck and Exir Chemical Companies and used without further purification. The solutions were prepared using methanol obtained from Zagros Petrochemical.

*2.1.1. Synthesis of (**1**) as single crystal and submicro-structured (**1′**) under ultrasound irradiation*

4,4'-bipyridine (**L**) (0.0156 g, 0.1 mmol) and 4-carboxybenzaldehyde (**HL′**) (0.0269 g, 0.1 mmol) were dissolved in 15 mL of ethanol. Then, $Cu(NO_3)_2$ (0.0374 g, 0.2 mmol) was dissolved in 5 mL deionized water and slowly added to the ligands solution. After 30 minutes of reaction under ultrasonic irradiation, the reaction mixture was filtered, and the resulting precipitate was carefully separated. The solid was subsequently washed with distilled water followed by ethanol to remove any residual impurities, and then dried under ambient conditions, the obtained powder of this reaction represented the desired submicro composite material (**1′**).

Subsequently, the clarified solution resulting from this reaction was left to stand for crystallization. After one-week, blue crystals were observed in the solution. These crystals were isolated and subjected to X-ray diffraction analysis to determine their structural characteristics (**1**). Hereafter, the single-crystalline bulk coordination polymer obtained from slow crystallization is

denoted as compound (**1**), whereas the sedimentary material prepared via ultrasound-assisted denoted as compound (**1′**).

2.2. Characterization instruments

The synthesized compounds were characterized using Fourier-transform infrared (FT-IR) spectroscopy recorded in KBr pellets on a JASCO FTIR-4600 instrument. Powder X-ray diffraction (PXRD) patterns were obtained using a Philips X'Pert diffractometer equipped with monochromatized Cu Kα radiation. The morphology of the samples was examined by scanning electron microscopy (SEM) using a TESCAN VEGA3 microscope. Thermogravimetric analysis (TGA) was performed on a PerkinElmer STA6000 apparatus. Ultrasonic-assisted reactions were carried out in a CLEAN ultrasonic bath.

2.2.1. X-ray crystallography

Single-crystal X-ray diffraction data for compound (**1**) were collected at room temperature using an Xcalibur four-circle κ-geometry diffractometer equipped with an Atlas CCD area detector and Mo Kα radiation (λ = 0.71073 Å) passed through a graphite monochromator. Data collection and unit-cell refinement were performed using the CrysAlisPro 1.171.42.93a software package. The crystal structure was solved by direct methods using SHELXS2014/5 and refined using SHELXL2018/3 with anisotropic displacement parameters applied to all non-hydrogen atoms. Absorption corrections were applied using the SCALE3 ABSPACK algorithm based on spherical harmonics.

Journal Pre-proof

Molecular graphics were generated using DIAMOND 3.0 and TOPOSPro, while the external morphology of crystals was predicted by the BFDH model implemented in VESTA. Hirshfeld surface mappings and 2D fingerprint plots were obtained using Crystal Explorer to analyze intermolecular interactions. The final least-squares refinement on F^2 converged to an R-factor of 0.042 for reflections with $F^2 > 2\sigma(F^2)$.

2.3. Hirshfeld surface analysis

Molecular Hirshfeld surfaces (HS) and the 2D fingerprint plots (FP) were calculated by using the Crystal Explorer [40] computer program with the input of X-ray crystallography data. The Hirshfeld surfaces were produced with a standard (high) surface resolution. It is possible to identify the areas of specific intermolecular interactions by using the normalized contact distance (d_{norm}), which is based on van der Waals radii, d_e (the distance from a point on the surface to the nearest atom outside the surface), and d_i (the distance from a point on the surface to the nearest atom inside the surface). The color scale for the 3D d_{norm} surfaces is fixed at -0.157 (red) to 1.279 Å (blue). Intermolecular interactions are either shorter or longer than van der Waals separations depending on whether d_{norm} is positive or negative. These surfaces are represented in 2D by fingerprint plots, which are shown by using the conventional 1.00 to 2.457 Å view with the d_e and d_i distance scales.

2.4. Biological studies

2.4.1. Antimicrobial activities (in vitro) by the well diffusion method

The compound's antibacterial effects were determined *in vitro* against gram-negative bacteria, *Pseudomonas aeruginosa* (ATCC: 9027), and *Escherichia coli* (ATCC: 25922), and positive

bacteria, *Bacillus subtilis* (ATCC: 6633) and *Staphylococcus aureus* (ATCC: 6538), using the well diffusion method. The trial samples were prepared in the sample tubes at specific concentrations (25, 50, and 100 mg/ml in DMSO). The plates were saturated with compound (**1′**) in the Muller Hinton Agar (Merck, Germany) medium, and the plates were then incubated at 37 °C. After 24 hours, the antibacterial activities were examined by measuring the diameter of the inhibition zone (in mm) from the growth that developed around the wells on the plates [41]. A blank bioassay verified that DMSO as a solvent had no action in our investigation, and Amoxicillin, Penicillin, and Cephalexin were chosen as reference bactericidal medications (positive controls) for any comparison under our conditions [42].

2.4.2. Antifungal activity by the disk diffusion method

The disk diffusion method was used to test for antifungals. The compound's antifungal qualities were examined against local isolates of *Candida albicans*. The disk was placed in different locations on the Sabouraud Dextrose Agar plate (Merck, Germany) that had been fecundated with one of the fungal spore suspensions after being soaked in chemical solutions at varying concentrations (25, 50, and 100 mg/ml in DMSO) [43]. For three days, *C. albicans* plate was incubated at 37 °C. The inhibition zone (mm) that developed around each disk during incubation was measured and noted as the compound's antifungal activity.

2.4.3. Determination of minimum inhibitory concentration (MIC) and minimum inhibitory bactericidal concentration (MBC)

MIC is the minimum inhibitory concentration needed to stop the bacteria's growth after 24 hours of incubation at 37 °C. We used the serial dilution approach to measure the MICs. MBC is the lowest concentration from which the bacteria do not grow when transferred to fresh medium. By

subculturing a loop full of broth dilution MIC tests to Muller-Hinton agar medium on the plate and then incubating it for 24 hours at 37 °C, MBCs were identified [44].

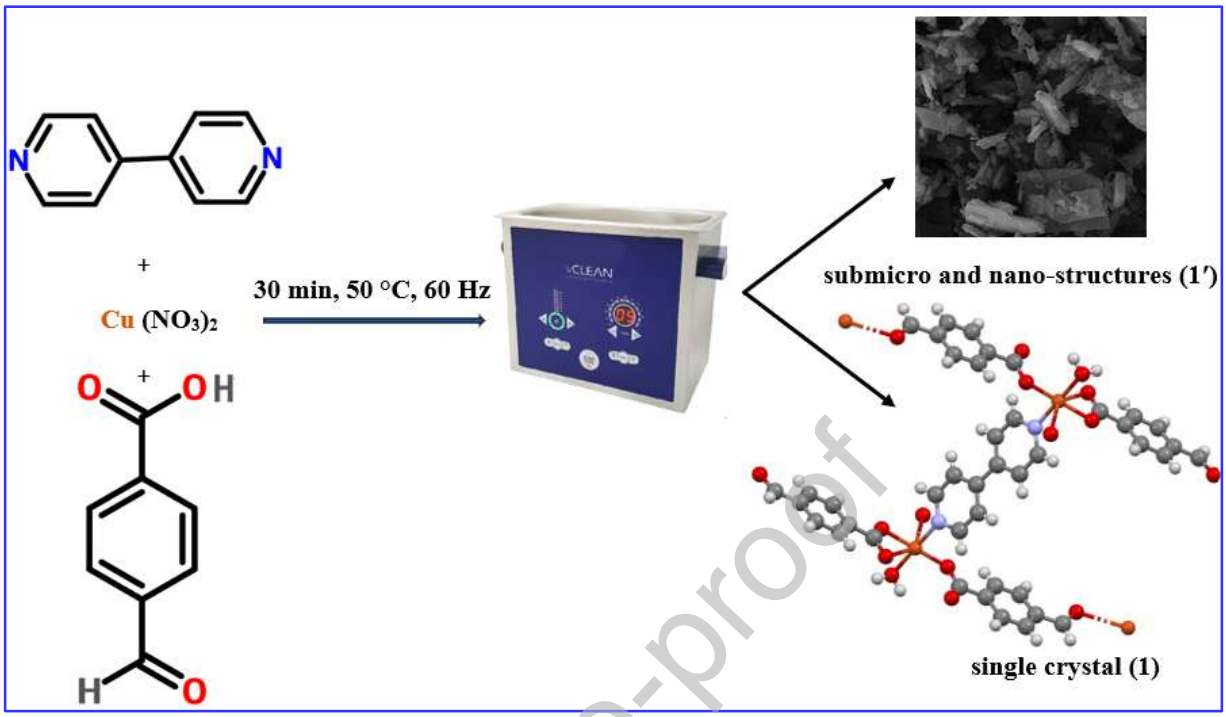
2.4.4. DNA cleavage test

The agarose gel electrophoresis technique was used to measure the compound's DNA cleavage potential while hydrogen peroxide (H_2O_2) was present as an oxidant (positive control). DNA was extracted as a substrate in accordance with previous reports [45]. In order to conduct the DNA cleavage test, the sample was incubated with 4 μL of the solution made by dissolving 5 mg of (**1′**) in 1 mL of DMSO and 4 μL of the extracted DNA (extracted by SINA COLON protocol). For two hours, the mixes were incubated at 37 °C. The trial sample was combined with bromophenol blue dye following incubation, and the standard DNA (alone), DNA and H_2O_2 mixture, and ladder were carefully inserted into the wells. For 30 minutes, gel electrophoresis was carried out at a constant 100 V. Following that, bands of DNA breakage were seen under UV light (transilluminator) and captured by camera [46].

3. Results and discussion

3.1. Synthetic perspective

In general, the sonochemical method was used to produce the new single crystal (**1**) and submicro-structured **(1′)** of coordination compound from L and HL′ (L = 4,4'-bipyridine and HL′ = 4-carboxybenzaldehyde) in ethanol and $Cu(NO_3)_2$ in water (Scheme 1).



Scheme 1. The synthetic routes of (**1**) and (**1′**).

3.2. Crystal structure analysis

3.2.1. Single-Crystal X-ray Diffraction (SCXRD) Analysis

The crystal structure of (**1**) was determined by single-crystal X-ray diffraction analysis, revealing a coordination polymeric framework constructed from Cu(II) centers and organic linkers (Table 1).

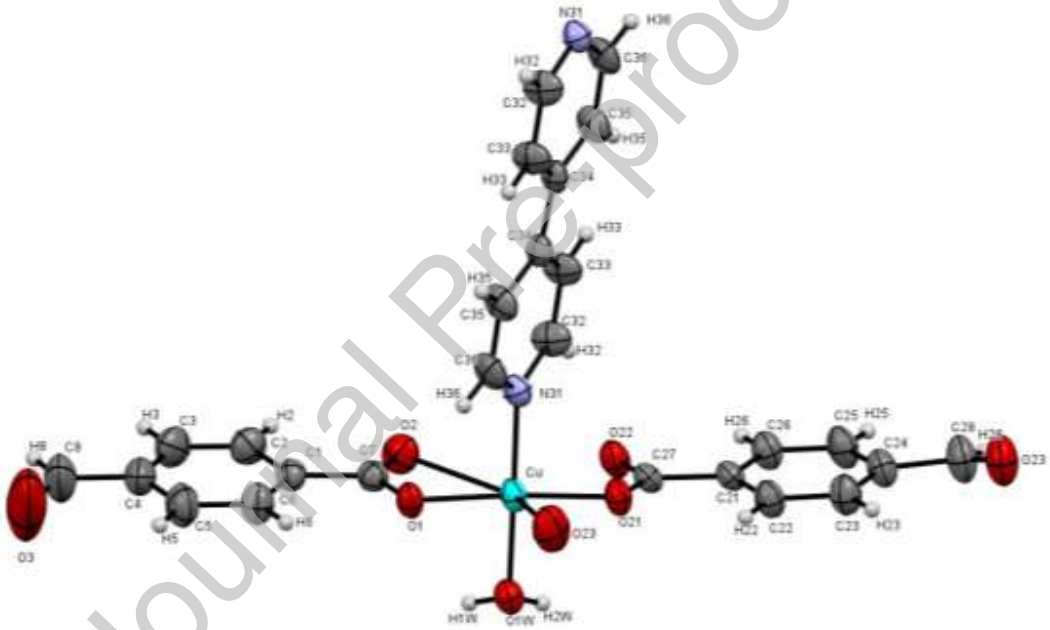
Journal Pre-proof

Table 1. Crystallographic information and structure refinement of compound (**1**).

Chemical formula	$C_{21}H_{16}CuNO_7$
Mr	457.89
Crystal system, space group	Monoclinic, $P2_1/c$
Temperature (K)	295
a, *b*, *c* (Å)	10.3831 (3), 12.6453 (3), 14.8052 (4)
α (°)	90
β (°)	96.430 (2)
γ (°)	90
V (Å^3)	1931.66 (9)
Z	4
Radiation type	Mo *K*α
μ (mm^{-1})	1.18
Crystal size (mm)	0.25 × 0.21 × 0.17
T_{min}, T_{max}	0.728, 1.000
observed [$I > 2\sigma(I)$] reflections	51959, 5062, 3698
R_{int}	0.063
$(\sin \theta/\lambda)_{max}$ (Å^{-1})	0.690
$R[F^2 > 2\sigma(F^2)]$, $wR(F^2)$, S	0.042, 0.110, 1.04
$\Delta_{\rho max}$, $\Delta\rho_{min}$ (e Å^{-3})	0.57, −0.43

Single-crystal X-ray diffraction analysis revealed that (**1**) crystallizes in the monoclinic space group *P2₁/c*, containing one crystallographically independent Cu(II) center coordinated by one carboxylic oxygen atom from 4-carboxybenzaldehyde, two oxygen atoms from another 4-carboxybenzaldehyde, one aldehyde oxygen atom from 4-carboxybenzaldehyde, one oxygen atom from H_2O and one nitrogen atom from bipyridine (Figure 1). The bond lengths are measured as follows: Cu-O21 at 1.940(16), Cu-O1 at 1.943(16), Cu-O2 at 2.747, Cu-O23 at 2.611, Cu-O1W at 1.975(17), and Cu–N31 at 2.005(2) Å (Table 2). The angles surrounding the Cu(II) center are

recorded as O21-Cu-O1 at 175.12(7)°, O21-Cu-O1W at 88.62(7), O1-Cu-O1W at 88.95(7)°, O21-Cu-N31 at 90.93(8)°, and O1W-Cu-N31 at 177.85(8)°. These findings suggest a twisted octahedral geometry for the structure, with Cu exhibiting a coordination number of six (Figure 2). The coordination environment around the Cu(II) center can be described as a distorted octahedral geometry, which is commonly observed for Jahn–Teller active d^9 copper(II) systems. Deviations from ideal octahedral geometry likely arise from ligand bite angles and steric constraints imposed by the carboxylate groups (Figure 2).



Journal Pre-proof

Figure 1. ORTEP representation (50% probability ellipsoids) of the coordination environment around the Cu(II) in compound (**1**).

Table 2. The selected bond lengths (Å) and angles (°) in (**1**).

Bond lengths			
Cu-O21	1.940 (16)	C1-C7	1.503 (3)
Cu-O1	1.943 (16)	C2-C3	1.387 (4)
Cu-O1W	1.975 (17)	C5-C6	1.385 (4)
Cu-O2	2.747	C1-C6	1.382 (4)
Cu-N31	2.005 (2)	C3-C4	1.369 (5)
Cu-O23	2.611	C4-C5	1.383 (5)
C1-C2	1.387 (4)	C4-C8	1.462 (4)
C27-O22	1.245 (3)	C27-O21	1.269 (3)
C7-O2	1.241 (3)	C7-O1	1.278 (3)
C8-O3	1.248 (6)	C28-O23	1.211 (3)
Bond angles [°]			
O21-Cu-O1	175.12 (7)	C6-C1-C2	118.9 (2)
O21-Cu-O1W	88.62 (7)	C6-C1-C7	121.7 (2)
O1-Cu-O1W	88.95 (7)	C2-C1-C7	119.4 (2)
O21-Cu-N31	91.65 (8)	C1-C2-C3	120.7 (3)
O1-Cu-N31	90.93 (8)	C7-O1-Cu	110.10 (15)
O1W-Cu-N31	177.85 (8)	C32-N31-Cu	122.37 (17)
C6-C1-C2-C3	1.0 (4)	C2-C3-C4-C8	178.80 (3)
C7-C1-C2-C3	−177.50 (3)	C3-C4-C5-C6	0.0 (5)
C2-C3-C4-C5	−0.30 (5)	C8-C4-C5-C6	−179.10 (3)

Symmetry code: (i) −x+1, −y+1, −z+2. Symmetry code: (ii) −x+1, −y+1, −z+1.

Journal Pre-proof

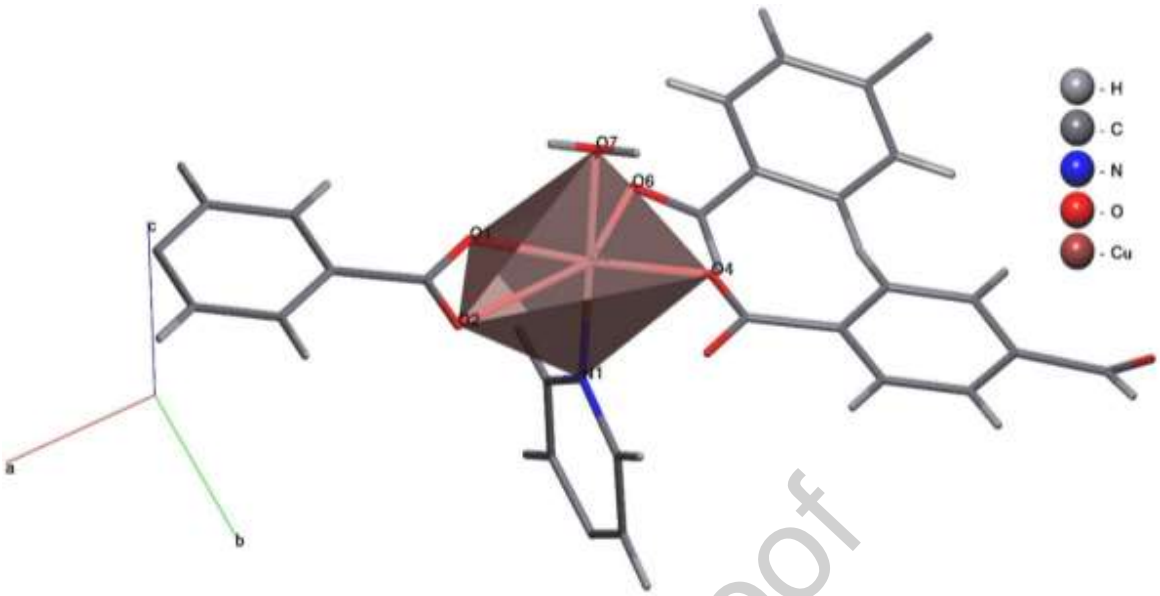


Figure 2. The geometrical sphere around the copper center in compound (**1**).

Bond lengths within the coordination environment, particularly Cu–O (1.940–1.975 Å) and Cu–N (2.005 Å), fall within the expected range for Cu(II) complexes featuring mixed N, O-donors (Table 2). The C–O distances in the carboxylate groups (1.221–1.301 Å) indicate significant π-delocalization, consistent with a π–π bridging mode. These structural parameters suggest a moderately rigid coordination sphere that stabilizes the 2D polymeric architecture (Figures 3, 4) [47].

3.2.2. Chemistry of Supramolecular Assemblies

The supramolecular organization of (**1**) is governed by a subtle yet highly coordinated interplay of non-covalent interactions, with hydrogen bonding and π–π stacking identified as the principal contributors to the stability of the extended architecture (Figures 3,4). Collectively, these

interactions generate a resilient two-dimensional framework that preserves the structural integrity and coherence of the crystal packing.

A detailed examination of the intermolecular landscape reveals a rich array of contacts, including conventional hydrogen bonds, van der Waals interactions, and intramolecular covalent constraints. Among these forces, hydrogen bonding clearly emerges as the dominant stabilizing factor. The carboxylate group of the 4-carboxybenzaldehyde ligand forms directional hydrogen bonds both with neighboring carboxylate functionalities and with the nitrogen donor sites of the 4,4′-bipyridine ligand (Figure 3). The associated donor–acceptor distances and bond angles fall well within the typical range for strong hydrogen bonds, underscoring their structural significance and reinforcing the connectivity of the coordination polymer.

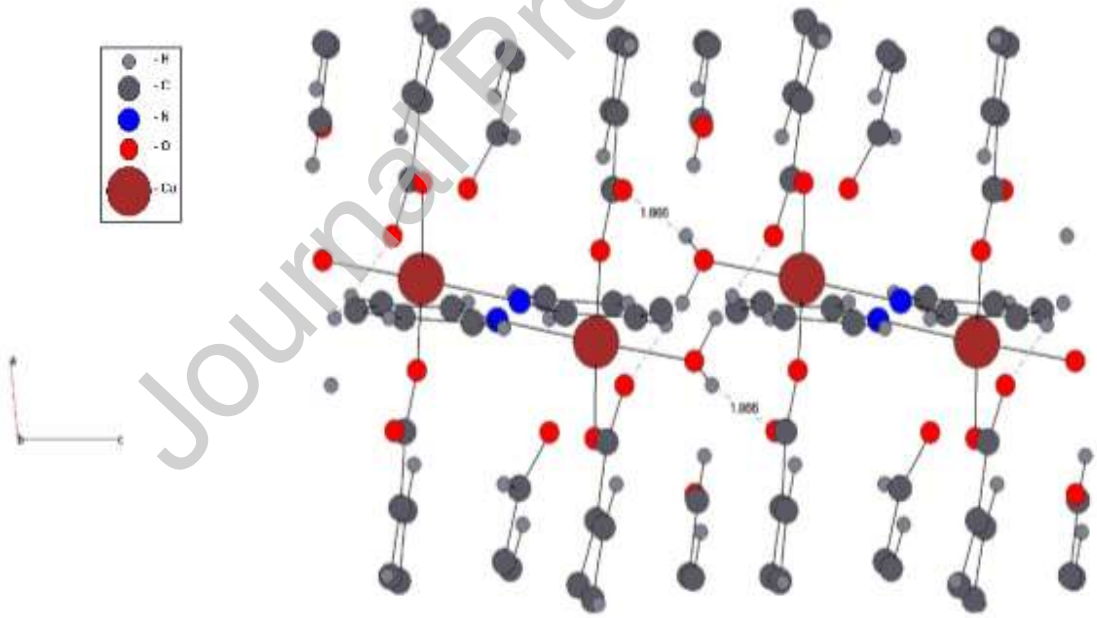


Figure 3. H-bonds interaction of compound (**1**).

Journal Pre-proof

A key feature of the supramolecular assembly is the involvement of water molecules, which function as efficient bridging agents linking adjacent fragments of the framework. Two notable intermolecular hydrogen bonds (H···O) are observed between ligand oxygen atoms and the hydrogen atoms of coordinated water molecules, with donor–acceptor separations of 2.663 Å and 2.690 Å (H1W···O22i and H2W···O2i, respectively). The hydrogen bonding geometry of compound (**1**), including relevant distances and angles, is detailed in Table S1. These interactions exhibit directional geometries characteristic of strong hydrogen bonds and highlight the essential role of water in consolidating the two-dimensional network.

In addition to hydrogen bonding, van der Waals interactions furnish supplementary cohesion to the lattice (Figure 4). Although individually weak, their cumulative effect enhances packing efficiency and contributes to the overall robustness of the supramolecular assembly. Furthermore, π–π stacking interactions between the aromatic rings of both ligands provide an additional layer of long-range stabilization (Figures 4a,b). The centroid–centroid distances and ring-slippage parameters fall within the expected range for effective stacking, thereby reinforcing the extended crystal architecture.

Journal Pre-proof

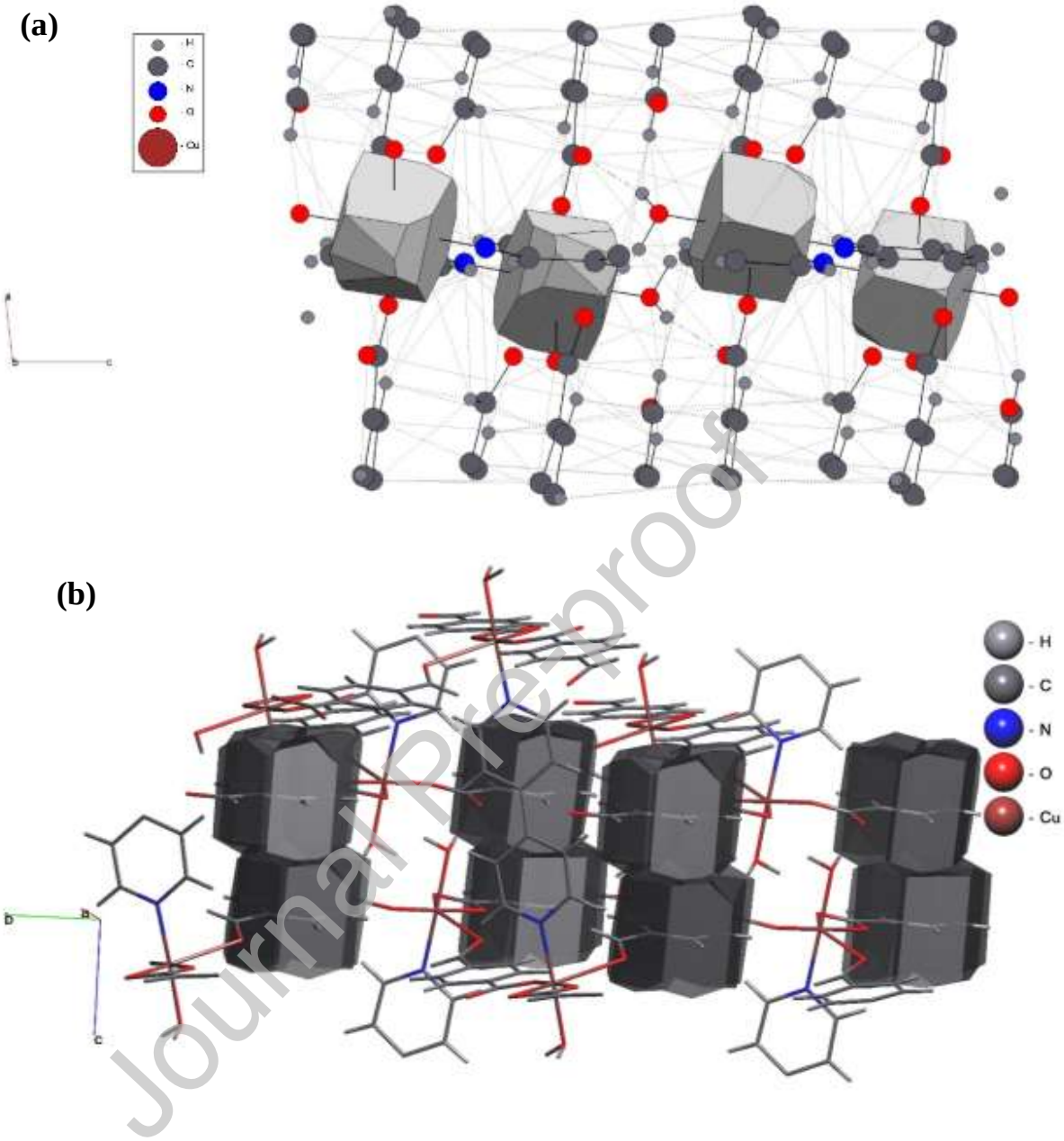


Figure 4. (a) The van der Waals interaction of compound (**1**) and (b) The π-π interaction of compound (**1**)

Taken together, the cooperative contributions of hydrogen bonding, π–π stacking, and van der Waals contacts culminate in a well-organized and structurally resilient supramolecular framework. This intricate network not only stabilizes the crystal lattice but also exemplifies the critical

influence of non-covalent forces in the rational design of advanced supramolecular and coordination polymer architectures. Two general views of compound (**1**) along the *ab* and *ac* crystallographic planes are shown in Figures S1a and S1b, respectively.

The Jahn–Teller distortion in compound (**1**) causes axial Cu–O elongation and slight equatorial asymmetry due to different donor strengths of O and N atoms. The two equatorial Cu–O bonds to carboxylates are nearly equal [1.940(2) and 1.943(1) Å], while Cu–O1W [1.975(2) Å] and Cu–N31 [2.005(2) Å] show variation. This asymmetry is consistent with e_g orbital splitting in a tetragonally distorted octahedral field. The stabilization energy is ~15–20 kJ/mol. Axial elongation reduces ligand field splitting along that axis, affecting d-orbital energy levels and the Cu(II)/Cu(I) redox potential.

A comparative structural analysis with related Cu(II) coordination polymers focuses on coordination geometry, space group, topology, dimensionality, and Jahn–Teller distortion, covering monomers to 1D and 3D networks with similar N-donor (bipyridines, imidazoles) and O-donor (carboxylates, formates, sulfates, nitrates) ligands (Table S2) [48–52]**.**

For comparison, the 1D polymeric complex $[Cu(4,4'\text{-bipy})(H_2O)_3(SO_4)].2H_2O$ reported by Phetmung et al. exhibits a similar 4+2 Jahn–Teller distorted octahedral geometry with equatorial Cu–N bonds of 2.0499(18) and 2.0487(17) Å, and axial Cu–O bonds of 2.2178(17) and 2.668(2) Å. The axial elongation in this compound (0.45–0.62 Å) is slightly less pronounced than in compound (**1**), which may be attributed to the different ligand field strength of sulfate compared to carboxylate ligands [48].

Similarly, the $[Cu(2,2'\text{-bipy})(NO_3)(H_2O)_3]NO_3$ complex reported by Kumar et al. exhibits a distorted octahedral geometry with Cu–N bonds of 2.0509(18) and 2.0697(18) Å, equatorial Cu–

O bonds of 2.0568(16), 2.0755(17), and 2.0808(16) Å, and a longer axial Cu–O bond of 2.0815(15) Å. The Jahn–Teller distortion in this complex is less pronounced due to the presence of a bidentate nitrate ligand that occupies equatorial positions, reducing the degree of tetragonal elongation [50].

The [CuCl(2-Me-imidH)$_4$]Cl complex reported by Atria et al. adopts a square-pyramidal geometry (τ_5 = 0.045) rather than an octahedral geometry, with four equatorial Cu–N bonds of 2.027(3) Å and an apical Cu–Cl bond of 2.627(3) Å. The presence of a chloride counterion at a non-bonding distance of 4.106 Å completes an imaginary elongated octahedron [51]. This geometry represents a more extreme case of Jahn–Teller distortion where the sixth coordination site is essentially vacant, highlighting the flexibility of Cu(II) coordination environments (Table 3).

Table 3. Comparison of coordination geometries and distortion parameters

Compound	Geometry	Cu–N(Å)	Cu–O(Å)	Cu–O/N(Å)	Jahn–Teller Elongation (Å)	Ref.
[Cu(4,4'-bipy)(H_2O)$_3$(SO_4)]·2H_2O	Distorted octahedral	2.049	1.964–1.981	2.218–2.668	0.45–0.62	[48]
[Cu(2,2'-bipy)(NO_3)(H_2O)$_3$]NO_3	Distorted octahedral	2.051–2.070	2.057–2.081	2.082	0.01–0.03	[50]
[CuCl(2-Me-imidH)$_4$]Cl	Square-pyramidal	2.027	–	2.627 (Cu–Cl)	–	[51]
[Cu(4,4'-bipy)(H_2O)$_3$(SO_4)].2H_2O (Polymorph)	Distorted octahedral	2.047–2.050	1.960–1.982	2.218–2.688	0.45–0.62	[52]
Compound (**1′**)	Distorted octahedral	2.005	1.943–1.975	2.611–2.747	0.65–0.80	This work

Journal Pre-proof

Compound (**1**) shows the smallest distortion ($\Delta \approx 0.035$ Å), indicating a weak Jahn–Teller effect. Equatorial Cu–O bonds are nearly equal (1.940–1.943 Å); Cu–N31 (2.005 Å) is slightly longer due to weaker N donor strength. Axial Cu–O1W (1.975 Å) is much shorter than typical axial bonds (2.15–2.65 Å), suggesting less elongation. [CuCl(2-Me-imidH)$_4$]Cl shows the strongest distortion (Δ = 0.64 Å) due to the long Cu–Cl bond [51]. Geometries range from square-pyramidal to distorted octahedral, with distortion correlating with axial ligand donor strength (Table S3) [49–52].

In compound (**1**), 2D layered network with distorted octahedral topology is created. Cu(II) centers are bridged by 4,4'-bipyridine in two directions, forming square grids. 4-carboxybenzaldehyde ligands coordinate terminally via carboxylate groups; aldehyde groups remain uncoordinated and form H-bonds stabilizing the 3D supramolecular architecture.

In [Cu(4,4'-bpy)(H_2O)$_3$(SO_4)]·2H_2O 1D zigzag chain, 4,4'-bipyridine bridges Cu along c-axis; sulfate is monodentate; three water molecules complete octahedral coordination. Chains interconnect via H-bonds (sulfate, coordinated/lattice water) forming a 3D supramolecular network with hexagonal cavities [48].

In [M(4,4'-bpy)(HCOO)$_2$(H_2O)]·4H_2O (M = Co, Ni) 3D porous framework, metal centers coordinated by two bridging 4,4'-bipyridine, two bridging formate, one terminal formate, and one water. Co-formate chains along (101); Co-bipyridine chains alternate along (110)/(1-10), forming 1D channels along (001) (~7.0 × 9.2 Å) [49].

In [Cu(2,2'-bipy)(NO_3)(H_2O)$_3$]NO_3 monomeric (0D) complex, Cu(II) coordinated by three water, one nitrate, and two N atoms from 2,2'-bipyridine. The second nitrate is non-coordinating and participates in H-bonding. Extensive H-bonding between adjacent molecules [50].

In [CuCl(2-Me-imidH)$_4$]Cl monomeric (0D) complex, Cu(II) ion with square-pyramidal geometry, is coordinated by four methylimidazole ligands in equatorial plane and one chloride at apex. Counterion chloride at non-bonding distance of 4.106 Å, forms an open 2D supramolecular network via H-bonds (Table S4) [51].

However, compound (**1**) is a 2D layered Cu(II) coordination polymer with distorted octahedral topology, crystallizing in the monoclinic space group $P2_1/c$. This distinguishes it from related 4,4'-bipyridine-based compounds, which typically crystallize in hexagonal ($P6_1$, $P6_5$) or trigonal (R-3c) space groups. The presence of the 4-carboxybenzaldehyde ligand is the primary factor influencing this difference, as its aldehyde group participates in hydrogen bonding and supramolecular packing. All Cu(II) compounds exhibit Jahn–Teller distorted octahedral geometries, but compound (**1**) shows a relatively large axial elongation (0.65–0.80 Å), indicating weaker axial interactions compared to [Cu(4,4'-bpy)$(H_2O)_3(SO_4)]\cdot 2H_2O$ (0.45–0.62 Å) [48]. In terms of dimensionality, compound (**1**) adopts a dense 2D structure with no significant porosity, in contrast to the 3D porous frameworks reported by Wang et al. [49] (void volumes of 26.5–33.9%). Other reference compounds include 1D zigzag chains [48], 3D formate-based networks [49], and 0D monomers [50,51]. The structural analysis confirms that compound (**1**) is a novel 2D Cu(II) polymer, and the ligand design plays a key role in tuning both the coordination geometry and supramolecular architecture.

3.2.3. Hirshfeld Surface Analysis

Intermolecular interactions within the crystal structure of compound (**1**) were examined through Hirshfeld surface analysis using Crystal Explorer 3.0. A key parameter in this analysis is d_{norm},

which reflects the symmetrical distance of a given point on the surface to nearby atomic centers both inside (d_i) and outside (d_e) the Hirshfeld surface relative to van der Waals radii. On the d_{norm} map, color coding helps visualize the strength and nature of interactions: red regions signify contacts shorter than the van der Waals radius, blue denotes longer contacts, and white indicates distances close to the expected van der Waals separation. Notably, various intensities of red ranging from pale to deep hues suggest weak to moderate intermolecular forces with adjacent molecules [53,54].

In addition to d_{norm}, the surfaces were analyzed with respect to parameters such as d_i, d_e, and curvedness, offering deeper insight into molecular packing (Figure 5). The associated figure illustrates key aspects of van der Waals contacts and bond interactions. These insights are further represented through 2D fingerprint plots, which combine d_i and d_e values to characterize interaction patterns and surface shape indices (Figure S3) [55,56].

Journal Pre-proof

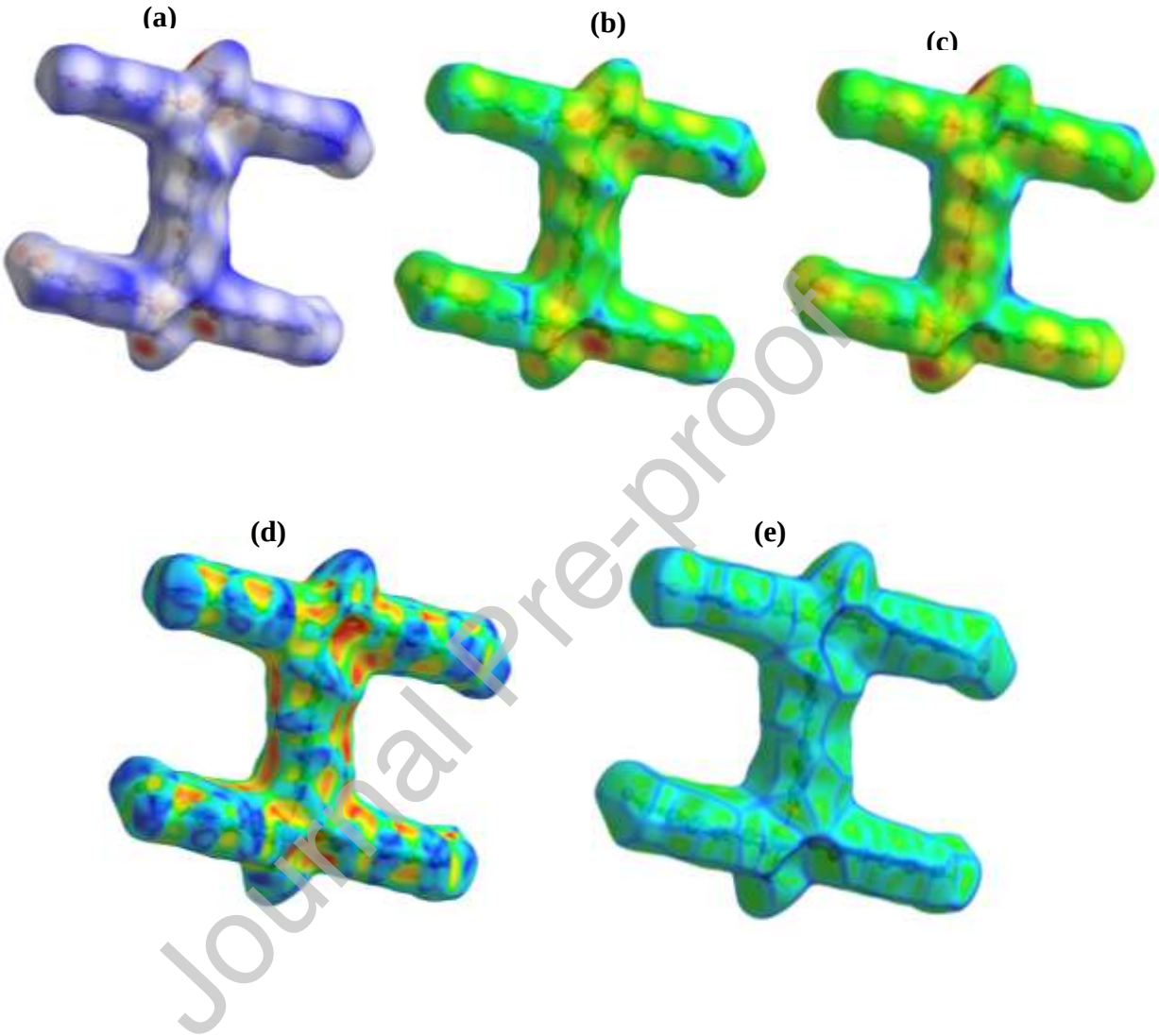


Figure 5. Hirshfeld surface analysis of compound (**1**): (a) Normalized distance (d_{norm}), (b) distance from a point on the Hirshfeld surface to the nearest external nucleus (d_e), (c) distance from a point on the Hirshfeld surface to the nearest internal nucleus (d_i), (d) shape Index, (e) curvedness

Journal Pre-proof

Figure 6 presents a chart of the percentage contributions of different intermolecular forces within the compound (**1**) crystal. The most dominant interaction was found to be H···H contacts, followed by O···H, C···H, Cu···O, and Cu···H interactions. Additionally, the occurrence of weaker O···O and O···C contacts was linked to the nature of the ligands involved.

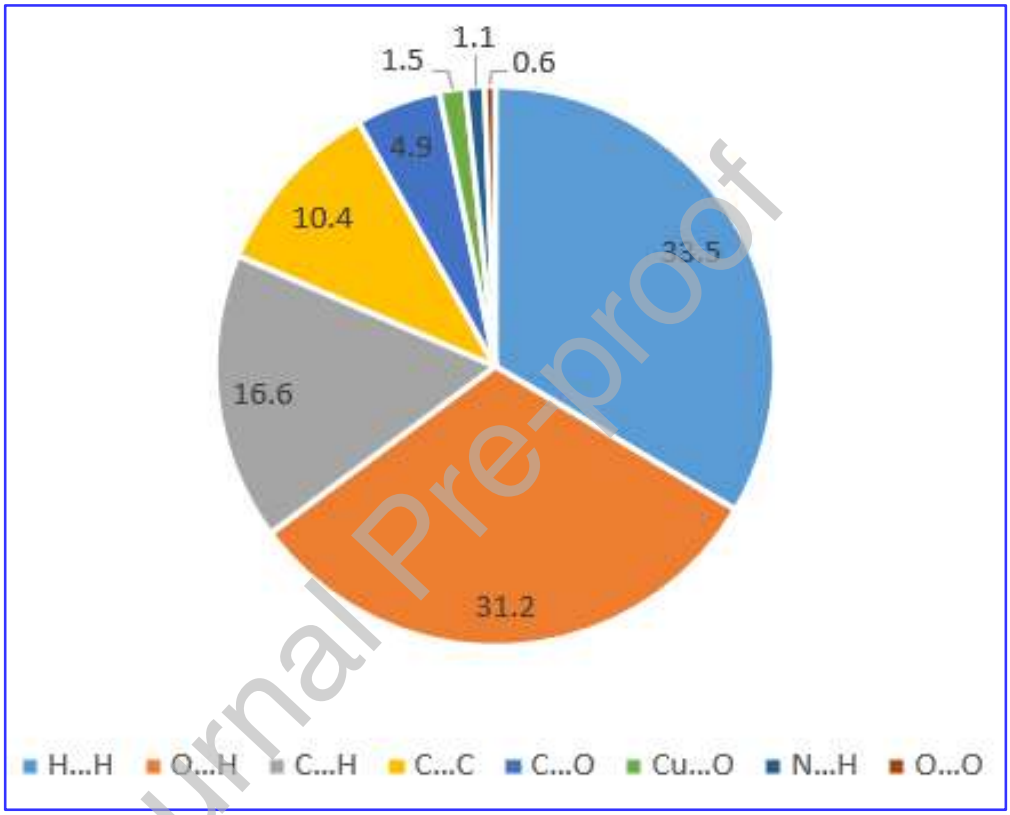


Figure 6. The relative contributions of compound (**1**) to the Hirshfeld surface area.

The Hirshfeld surface fingerprint plots of compound (**1**) show that H···H contacts constitute the highest proportion (33.5%) among all intermolecular interactions. However, these contacts are typically non-directional van der Waals interactions, reflecting spatial proximity rather than contributing significantly to structural cohesion. In contrast, O···H contacts, accounting for 31.2%

Journal Pre-proof

of the surface interactions, play a more decisive role in stabilizing the framework. These directional hydrogen bonds often formed between coordinated oxygen atoms as well as hydrogen donors from ligands or lattice solvents enhance the rigidity and integrity of the crystal lattice. Their prevalence underscores the importance of hydrogen bonding in reinforcing the 2D architecture of the coordination polymer, surpassing the mere abundance of H···H contacts in terms of structural impact (Figure 6). The distances d_{norm}, d_i, and d_e were calculated through the software (Table S5).

Beyond serving as a quantitative tool for describing crystal packing, Hirshfeld surface analysis also provides useful insight into how the framework may interact with polar environments. The relatively high contribution of O···H contacts points to the prominence of hydrogen-bond-related interactions at the molecular surface, which are well suited for interaction with hydrogen-bond-rich biological substrates such as DNA. From this perspective, the Hirshfeld analysis suggests that supramolecular surface features, in addition to the metal coordination core, may contribute to the DNA cleavage behavior observed for compound (**1′**).

Journal Pre-proof

3.3. Characterization of compound (1′)

3.3.1. FTIR Analysis

The FT-IR spectra were recorded to investigate the synthesis of compounds (**1**) and (**1′**) **(**Figure S**4**). The IR spectrum of the polymeric copper (II) complex shows several characteristic absorptions. The band at 2931 cm^{-1} corresponds to aromatic C–H stretching vibrations, confirming the preservation of the aromatic framework. In the free 4-carboxybenzaldehyde ligand, the C=O stretching vibration of the carboxylic acid is observed around 1700–1720 cm^{-1}**.** In the polymeric complex, these peaks related to C=N and C-O bonds appearing at 1560 cm^{-1} and 1290 cm^{-1}**,**

respectively. The band at 1560 cm^{-1}**,** which also overlaps with the C=N stretching of the bipyridine ligand (normally ~1595–1600 cm^{-1}), shifts to lower frequency upon coordination, indicating the formation of Cu–N bonds. The band at 1290 cm^{-1} is assigned to the C–O, confirming coordination of the carboxylate oxygen atoms and the presence of Cu–O bonds**.**

In addition, weak absorptions expected in the far-IR region provide further evidence of direct metal–ligand interactions: Cu–N stretching typically occurs between 400–500 cm^{-1}**,** while Cu–O stretching is observed in the 450–600 cm^{-1} range. Although these signals are often of low intensity, they support the proposed coordination environment around the copper center [57].

3.3.2. XRD Analysis

Figure 7 compares the simulated XRD pattern of compounds (**1**) and (**1′**), obtained from single-crystal X-ray diffraction data, with the experimental PXRD pattern of the submicro-structured synthesized via the sonochemical method. The strong agreement between the two patterns, particularly the close alignment of the major diffraction peaks, confirms that the crystalline phase of the sonochemically produced material is consistent with the structure determined from single-crystal analysis.

Distinct diffraction peaks appear at approximately 2θ = 12°, 14°, 15°, 16°, 17°, 19°, 25°, 28°, 30°, 31° and 36°, corresponding to the crystallographic planes (11–1), (020), (11-2), (120), (200), (013), (11-4), (040), (32-2), (204) and (24–1), respectively. The presence of these characteristic reflections verifies the successful formation of the Cu-based coordination polymer of compounds (**1**) and (**1′**) and confirms that no significant secondary crystalline phases are present in the

submicro-structured product. The excellent peak agreement further demonstrates that the ultrasonic-assisted synthesis preserves the integrity of the crystal framework obtained via SCXRD.

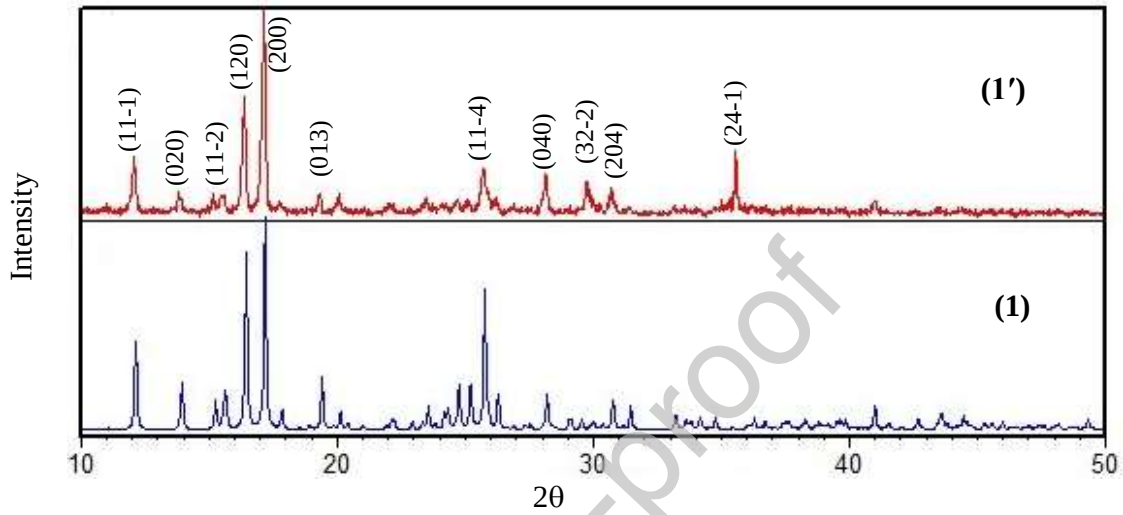


Figure 7. The PXRD patterns of (up) submicron-sized provided by ultrasonication compound (**1′**), and (bottom) simulated from single crystal X-ray data of compound (**1**).

The phase purity and structural integrity of the ultrasonication-synthesized submicron-sized compound (**1'**) were unambiguously confirmed by powder X-ray diffraction (PXRD). As illustrated in Figure 7, the experimental diffraction pattern of the submicro material (**1'**) (upper trace) is compared with the pattern simulated from the single-crystal X-ray data of compound (**1**) (lower trace). A detailed side-by-side analysis reveals an excellent match between the two patterns across the entire 2θ range (5–50°). All major Bragg reflections observed in the submicro sample, including those at low, intermediate, and high diffraction angles, are faithfully reproduced in the simulated pattern, with no discernible shifts in peak positions. Critically, the relative intensities of the dominant peaks particularly the most intense reflection and its adjacent shoulders are consistent

Journal Pre-proof

between the experimental and simulated diffractograms, confirming that the bulk submicro powder possesses the identical long-range ordered crystal lattice as the single crystal. The slight broadening observed in the experimental submicro sample peaks, compared to the sharper simulated peaks, is fully consistent with the reduced crystallite size and the effect of particle morphology at the submicro-scale (Scherrer broadening). Importantly, no extraneous peaks attributable to amorphous by-products, unreacted starting materials, or alternative crystalline polymorphs are detectable in the experimental pattern.

This near-perfect superimposition of the simulated and experimental diffractograms, both in terms of peak positions and relative intensities, provides conclusive evidence that: 1) The submicro-structured is phase-pure, 2) The crystal structure determined from the single crystal is truly representative of the bulk submicro material, 3) The ultrasonication process did not induce any phase transformation or degradation of the crystalline framework. Therefore, the PXRD data firmly establish that the submicron-sized compound (**1'**) retains the identical crystalline architecture as its single-crystal counterpart, validating both the synthesis protocol and the subsequent structural and property comparisons.

Journal Pre-proof

3.3.3. TGA Analysis

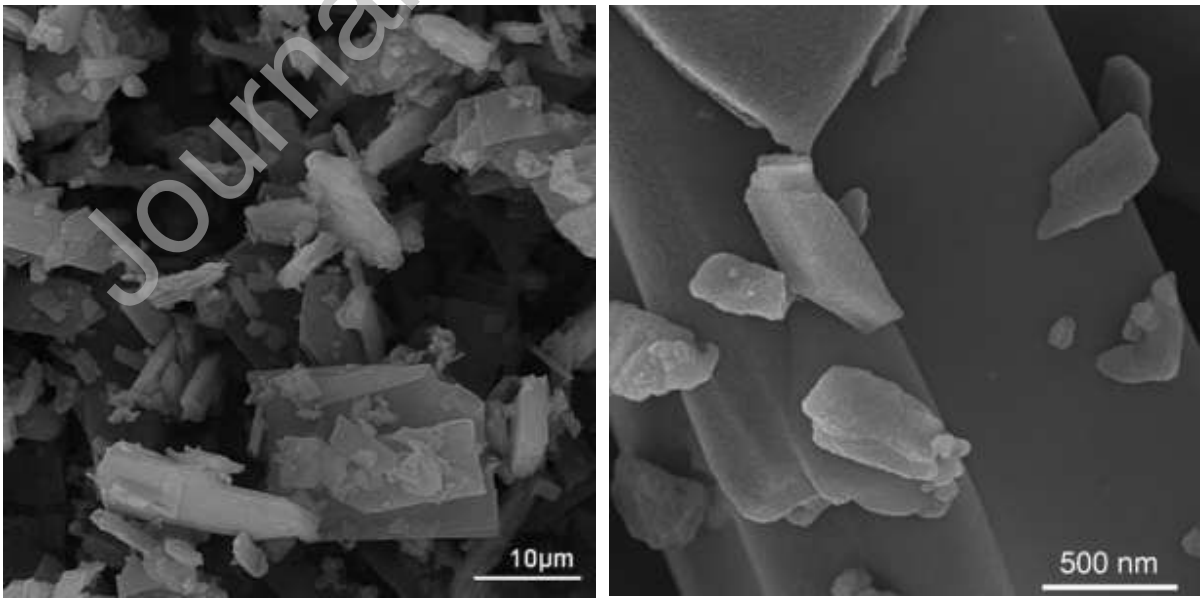
The thermal gravimetric analysis (TGA) was performed at 30-800 ℃ under neutral atmosphere (argon) protection to study the thermal activity of compound (**1**') (Figure S**5**). Compound (**1**') shows stability until 140 ℃. The TGA curve exhibits three temperature peaks in the range of 140-166 ℃, 240-305 ℃ and 305-800 ℃, corresponding to the loss of coordinated H_2O (Exp. ≈ 3.8%, Calc. = 3.9%), two carboxybenzaldehyde compounds (Exp. ≈ 57.5%, Calc. = 58.1%) and a half of

bipyridine compound (Exp. ≈ 16.0%, Calc. = 17.1%), respectively. The remaining material at 800 ℃ is $Cu(OH)_2$ (Exp. = 22.7%, Calc. = 21.3%), and as the temperature rises to 1000 ℃, there is a possibility of CuO formation.

*3.3.4. The Morphology of Submicro-Structured Compound (**1′**)*

The morphology of the submicro-structured compound (**1′**) was examined using SEM (Figure 8), revealing predominantly plate-like crystalline domains with sharp edges and well-defined layered surfaces. These plate-shaped structures arise from anisotropic crystal growth, which is consistent with the supramolecular packing interactions observed in the single-crystal structure, particularly π–π stacking and directional hydrogen bonding.

The submicro-material consists of aggregated clusters formed through the stacking of thin crystalline layers. ImageJ analysis of particle size distribution confirmed that the primary particles fall within the 127–150 nm range, indicating uniform nucleation during ultrasound-assisted synthesis.



Journal Pre-proof

Figure 8. SEM images of micro and submicron-size particles of (**1′**).

Such controlled submicro-scale morphology is significant because particle size and shape strongly influence surface area, biological interactions, and catalytic behavior. The thin plate-like morphology may facilitate enhanced contact with bacterial membranes or biological substrates, which could partially explain the compound's observed antimicrobial and DNA-cleavage activities. Overall, SEM analysis supports the formation of well-defined submicro-scale compound (**1′**) whose morphology correlates with both the crystallographic packing motifs and the material's functional properties.

From a functional standpoint, the plate-like morphology and the relatively narrow particle-size distribution of compound (**1′**) are of interest. Such morphological features can increase the accessible surface area and expose a larger portion of the coordination framework to the surrounding medium, potentially favoring surface-mediated interactions with biological substrates. While morphology alone cannot account for biological activity, the submicro-scale architecture of (**1′**) is expected to contribute to the DNA cleavage and antimicrobial responses observed under *in vitro* conditions.

3.3.5. Dynamic Light Scattering (DLS) and Particle Size Analysis

To complement the SEM observations and to clarify the hydrodynamic behavior of compound (**1′**) in solution, dynamic light scattering (DLS) measurements were performed in aqueous media. As presented in Figure S6, the DLS analysis revealed a mean hydrodynamic diameter of

approximately 490 nm with an excellent polydispersity index (PDI) of 0.010, indicating a highly monodisperse particle population in the colloidal state.

This result is particularly informative when compared to the SEM data, which show individual primary particles with diameters of 127–150 nm. The significant discrepancy between the dry-state size (SEM) and the larger hydrodynamic diameter (DLS) is attributed to two main factors: (i) the formation of stable submicron-sized aggregates or nanoclusters in aqueous solution, as supported by the remarkably low PDI value, and (ii) the inclusion of the hydration layer and surface ligands in the DLS measurement, which are collapsed during SEM sample preparation. Furthermore, the intensity-weighted distribution in DLS is inherently biased toward larger species, making it sensitive to the presence of even minor agglomerates.

Collectively, these results indicate that while the primary particles are in the sub-100 nm to 150 nm range (as confirmed by SEM), they exhibit a strong tendency to form stable aggregates in solution, resulting in an overall submicro-structured material with a hydrodynamic size of approximately 490 nm. This aggregation behavior is consistent with the plate-like morphology and the strong interparticle interactions (e.g., hydrogen bonding and π–π stacking) expected for this type of coordination polymer. Therefore, compound (**1′**) is best described as a submicro-structured material composed of aggregated primary particles, rather than discrete nanoparticles. This characterization is crucial for interpreting its biological activity, as the aggregation state in solution may influence cellular uptake and diffusion.

3.4. Frontier Molecular Orbital Analysis

Journal Pre-proof

We have performed molecular orbital calculations using the B3LYP/LANL2DZ method in Gaussian 3 (revision B.01) [58], that based on hybrid Density Functional Theory (DFT). In these calculations the 20 core electrons are modelled by pseudopotentials and the remaining 468 electrons are treated explicitly via molecular orbitals (MOs). The plots of the frontier MOs are shown in Figure 9 and we obtained at 0.02 e/bohr^3 isosurface, overlayed onto a fragment of the Cu-MOF that contains two copper centers, one 4,4'-bipyridine linker and four 4-formylbenzoate linkers in addition to one water molecules on each copper center. These structures were fully optimized without any constraints and confirmed via vibrational analysis, to be minima on the potential energy surface, due to the absence of imaginary vibrational frequencies.

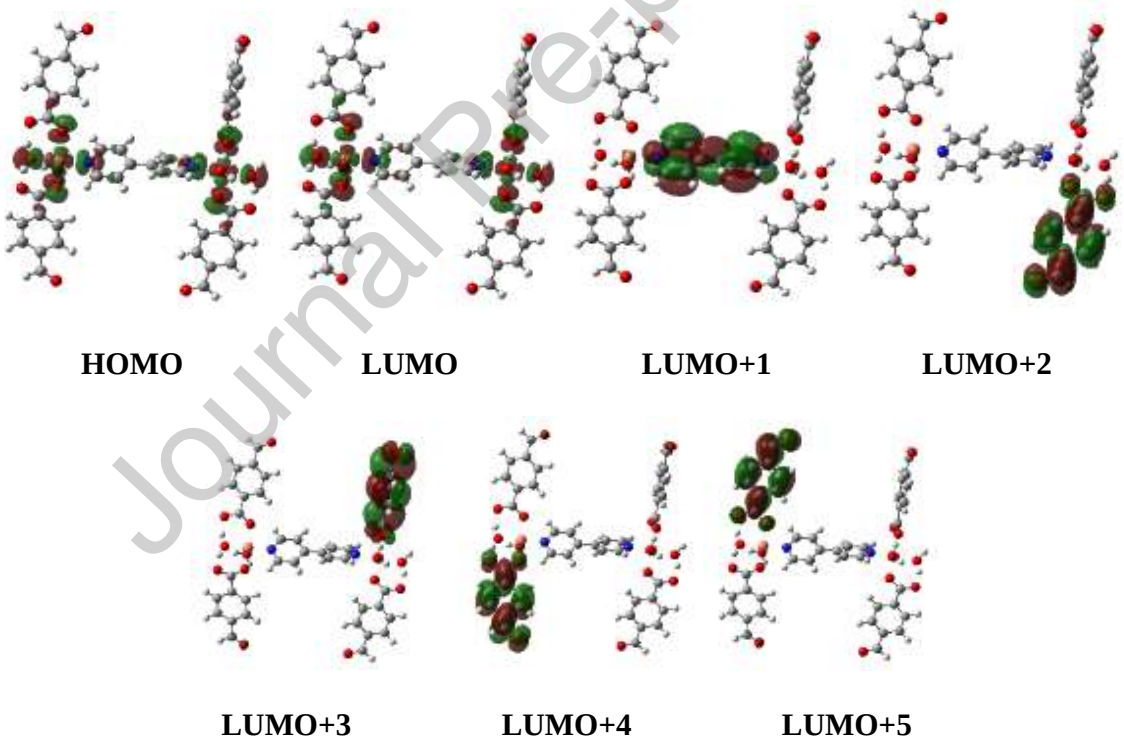


Figure 9. Frontier Molecular Orbital Analysis of (**1**) fragment**.**

Journal Pre-proof

The HOMO and LUMO orbitals have the same spatial distribution with a change in the wavefunction sign. These MOs are primarily located on the copper atoms as filled d-states that are either d_{xy}, d_{yz}, and d_{xz} symmetry, hybridized with p-orbitals on the adjacent nitrogens of 4,4'-bipyridine linker and oxygens of the 4-formylbenzoate linkers. The bandgap for this fully optimized molecular structure was found to be 0.265 eV, which indicates that in a desolvated environment this Cu-MOF is a narrow bandgap semiconductor that could absorb mid-infrared electromagnetic radiation of about 5170 nm, that could initiate photocatalytic reactions at the copper centers with gas phase molecules, within the porous structure of this material.

Furthermore, the LUMO+1 state appears to be a quinoid π-state on the 4,4'-bipyridine linker close to the Fermi level of this Cu-MOF, which indicates an extended conjugated π-system, that could transfer electrical currents between copper centers, in the direction that 4,4'-bipyridine linker connect the Cu centers. The electromagnetic radiation that would enhance such electron transfer was found in the visible range of the spectrum (λ = 500 nm, green light), which would become an important parameter in the application of such structures as visible light photocatalysts.

Additionally, in the direction of the 4-formylbenzoate linkers, the bandgap excitations of this semiconductor were found to be in Vis-violet region of electromagnetic spectrum at 389 - 405 nm. These virtual states (LUMO+2, LUMO+3, LUMO+4, LUMO+5) were found to be conjugated a quinoid π-state which indicates conductivity along this direction of the MOF if excited by photons with wavelengths of 389–405 nm. This indicates that this Cu-MOF will have properties of a narrow bandgap semiconductor for photocatalytic reactions occurring at the copper centers, however, the macroscopic structure of this MOF will have semiconducting properties with a bandgap of about 2.48 eV, which may become important for visible spectrum photoinduced excitations and potential electron transfer within the Cu-MOF framework at λ = 500 nm, green light.

Journal Pre-proof

Journal Pre-proof

3.5. Antimicrobial bioassay (*in vitro*)

Two kinds of bacteria, *B. subtilis* and *S. aureus* being Gram-positive bacteria and *E. coli* and *P. aeruginosa* being Gram-negative bacteria, were chosen in order to examine the compound's antibacterial properties submicro-particles of (**1′**) inhibited bacterial growth, with inhibition zones ranging from 6.00 mm to 9.26 mm (Figure 10, Table 4). The medication actions of some common antibiotics, including cephalexin, amoxicillin, and penicillin, against the mentioned bacteria were also investigated in our conditions in order to compare the outcomes (Table 4). Overall, the findings suggest that the substance possesses antimicrobial properties. The compound's antibacterial activity increased at larger doses. The compound's antibacterial activity is highest against *E. coli* and lowest against *S. aureus*. When comparing the compound's antibacterial activity to that of conventional medications, it is found that while the compound's antibacterial activity is lower, it nevertheless effectively inhibits the development of germs.

The antifungal effectiveness of compound (**1′**) was tested against *Candida albicans*. Growth inhibition zones of 6, 6, and 7 mm were observed at concentrations of 25, 50, and 100 mL of the compound, respectively (Figure 10).

The antibacterial activity of compound (**1′**) was systematically evaluated against both Gram-negative *(E. coli, P. aeruginosa*) and gram-positive (*B. subtilis, S. aureus*) strains. The inhibition zones increased with concentration, reaching a maximum of 9.26 mm for *S. aureus* at 100 mg/mL, indicating that Gram-positive bacteria were much susceptible than Gram-negative ones.

It is worth noting that inhibition zone diameters obtained from diffusion-based assays are affected by several factors beyond the intrinsic antibacterial activity of a compound, including its solubility, diffusion behavior in the agar medium, and particle size. Consequently, inhibition zones

should be interpreted with care when comparing different bacterial strains. In the present study, although *S. aureus* displayed the largest inhibition zone at higher concentrations, the antibacterial response of compound (**1′**) was found to depend on the method used for evaluation.

To obtain a more reliable and quantitative assessment of antibacterial performance under liquid-phase conditions, MIC and MBC measurements were therefore carried out. While the antibacterial activity of compound (**1′**) remains lower than that of standard antibiotics, the observed inhibitory effect is clearly detectable and provides a reasonable starting point for further optimization.

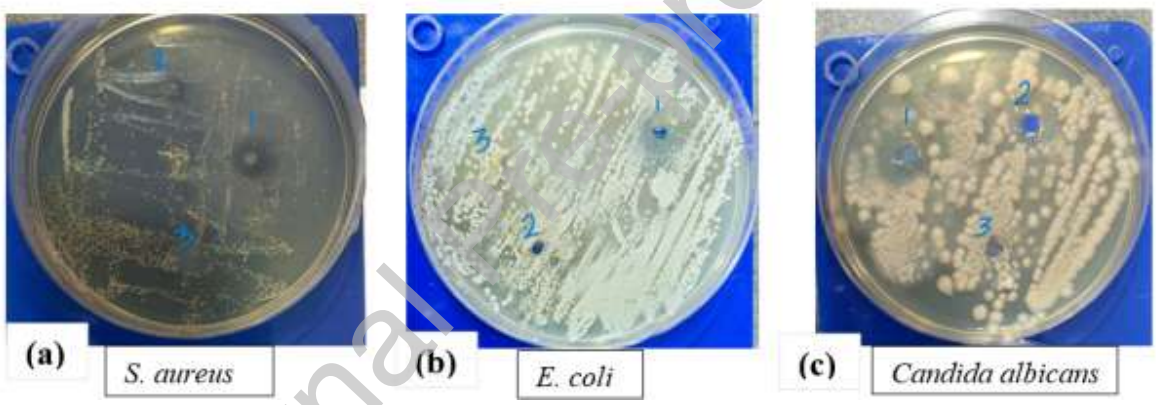


Figure 10. Antimicrobial activity assay by disk diffusion method: (**a**) The inhibition zone produced by *S. aureus* bacteria, when exposed to submicro compound (100, 50, and 25 mg/mL in DMSO), (**b**) The inhibitory zone observed for *E. coli* bacteria treated with the submicro-particle (100, 50, and 25 mg/mL in DMSO). (**c**) The inhibition zone generated by *Candida albicans* fungus upon treatment with the submicro-particle (100, 50, and 25 mg/mL in DMSO).

3.6. MIC and MBC Studies of (1′)

Mueller-Hinton broth was also used to evaluate the compound's MIC and MBC values for more precision in our investigations (Table 4). According to the results, the chemical is effective against the bacterial strains indicated, with MBC values for *B. subtilis*, *S. aureus*, *P. aeruginosa*, and *E. coli* being 9, 25, 1, and 12 µg/mL, respectively. *B. subtilis*, *S. aureus*, *P. aeruginosa*, and *E. coli* were found to have MIC values of 98, 25, 97, and 125 µg/mL, respectively. MBC and MIC data indicate that the most inhibitive toward the growth of *P. aeruginosa* and *B. subtilis*.

Table 4. Antibacterial activities of (**1′**) and antibiotic drug on various bacteria.

Bacteria	Gram (-) bacteria						Gram (+) bacteria					
	E. coli			*P. aeruginosa*			*B. subtilis*			*S. aureus*		
Concentration (mg/mL)	25	50	100	25	50	100	25	50	100	25	50	100
Zone of inhibition (mm)	6.34	7.53	8.12	6.00	7.36	7.45	6.00	7.56	3.12	00	8.09	9.26
MIC (µg/mL)	125			97			98			25		
MBC (µg/mL)	12			1			9			25		
Amoxicillin (25 mg/disk)	20.80			18.78			28.10			41.60		
Penicillin (10 mg/disk)	9.70			19.32			30.50			47.40		
Cephalexin (30 mg/disk)	22.56			16.32			37.60			41.60		

MIC and MBC values further supported this observation, with *S. aureus* showing the lowest MIC (25 µg/mL), while *P. aeruginosa* exhibited the lowest MBC (1 µg/mL), suggesting strong bactericidal activity at low concentrations. Although the inhibition zones of (**1′**) were smaller compared to standard antibiotics such as amoxicillin, penicillin, and cephalexin, the polymer

demonstrated promising antibacterial potential considering its synthetic origin and multifunctional framework. Any direct comparison with previously reported coordination polymers should be approached with caution, as differences in experimental protocols and testing conditions can strongly influence MIC and MBC values. Within this context, the MIC/MBC data obtained for compound (**1′**) fall within the range typically reported for Cu-based coordination systems examined under comparable *in vitro* conditions [59].

The MIC and MBC measurements offer a more quantitative view of the antibacterial performance of compound (**1′**) in liquid media. The variations observed among different bacterial strains are consistent with known differences in cell wall architecture, metabolic activity, and sensitivity toward metal-containing compounds. Taken together with the diffusion-based assays, these results indicate that compound (**1′**) displays measurable bacteriostatic and bactericidal effects that depend on both the microorganism and the applied concentrations.

Overall, while compound (**1′**) does not approach the potency of conventional antibiotics, the MIC/MBC findings, considered alongside its pronounced DNA cleavage activity, suggest that its antibacterial action cannot be attributed solely to diffusion-related effects.

Journal Pre-proof

3.7. DNA Cleavage Potential

The DNA cleavage ability of compound (**1′**) was evaluated using agarose gel electrophoresis with DNA extracted from *Candida albicans*. As shown in Figure 11a, lane assignments were as follows: **L** (DNA ladder), **P** (control DNA), **H** (DNA + H_2O_2, positive control), and **C** (DNA + compound (**1′**)). In lane P, intact DNA bands were clearly visible, whereas lane H demonstrated complete DNA degradation due to oxidative cleavage by H_2O_2. Strikingly, lane C revealed a similar disappearance of DNA bands, indicating that compound (**1′**) possesses strong DNA cleavage

activity comparable to H_2O_2. These findings suggest that, although the compound exhibits limited cell penetration based on growth inhibition zone data, once inside *Candida albicans* cells it can effectively induce DNA strand scission.

A parallel experiment was conducted with DNA extracted from *Escherichia coli* (Figure 11b). The lane assignments were identical to those described above. Again, lane P displayed intact DNA, while lane H confirmed complete oxidative cleavage by H_2O_2. Lane C showed the absence of DNA bands, demonstrating that compound (**1′**) is capable of inducing extensive DNA cleavage in *E. coli* as well. Thus, despite its relatively low ability to infiltrate bacterial cells, the compound exhibits pronounced nuclease-like activity once cellular entry is achieved.

The observed DNA cleavage activity of compound (**1′**) aligns with reports on other coordination compounds and metal–organic polymers that act as artificial nucleases. For example, copper(II) coordination polymers containing phenanthroline and azopyridine ligands have been shown to cleave plasmid DNA through oxidative mechanisms involving hydroxyl and superoxide radicals [60]. Similarly, sulfadoxine-based silver and platinum complexes demonstrated complete cleavage of calf thymus DNA, highlighting the role of transition metals in enhancing nuclease activity [61]. In another study, complexes tested in the presence of H_2O_2 converted supercoiled DNA into nicked and linear forms, confirming their oxidative cleavage potential.

Compared to these systems, (**1′**) exhibits comparable efficiency to H_2O_2 in direct DNA cleavage, but its cellular uptake appears more restricted, as inferred from antimicrobial zone of inhibition data. This duality high nuclease activity but limited penetration distinguishes (**1′**) from other reported complexes that often combine strong DNA cleavage with broader antimicrobial activity. Such findings emphasize the importance of both intrinsic nuclease potential and cell

Journal Pre-proof

permeability in evaluating the biological relevance of coordination compounds. The DNA cleavage behavior observed in this study is most reasonably attributed to an oxidative pathway, in which the Cu(II) center undergoes redox processes in the presence of an oxidant, giving rise to reactive species capable of inducing strand scission. Similar oxidative mechanisms have been proposed for other copper-based coordination compounds that function as artificial nucleases. It should be noted, however, that a detailed mechanistic investigation would be necessary to clearly identify the specific reactive intermediates involved [46].

Within this context, the pronounced DNA-cleaving activity observed for compound (**1′**) provides a plausible explanation for its antibacterial effect, particularly when sufficient interaction with genetic material takes place. Nonetheless, diffusion-based assays indicate that its overall potency remains relatively modest.

Journal Pre-proof

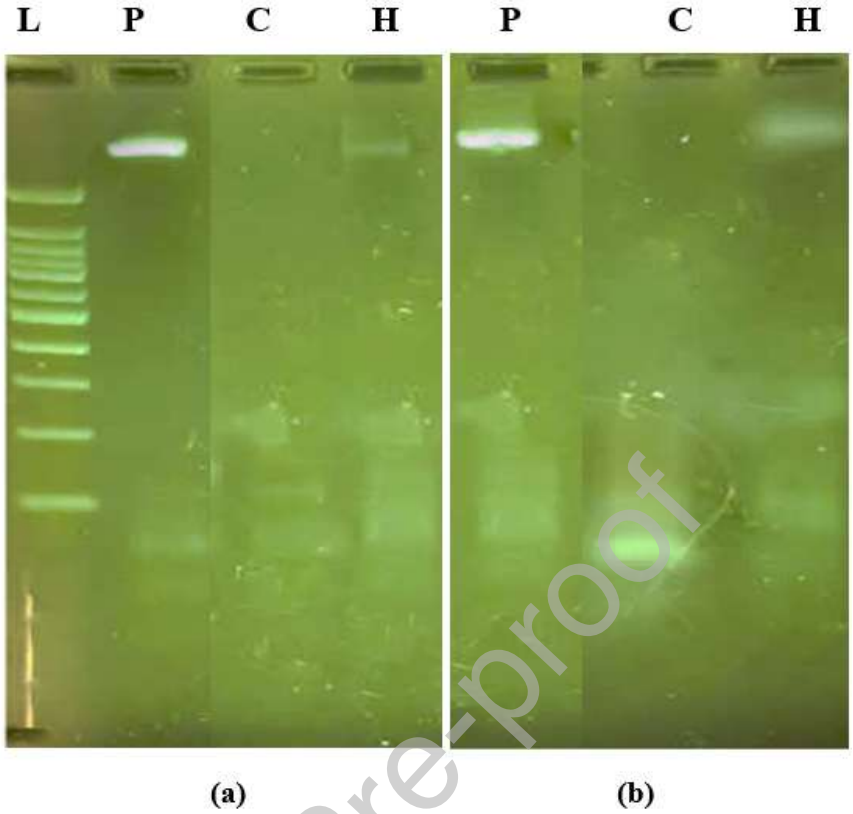


Figure 11. Gel electrophoresis picture **a)** *C. albicans* and **b)** *E. coli* for DNA cleavage of compound (**1′**). **L**, the ladder, **P**, the control DNA (DNA only), and **C**, compound (**1′**) plus DNA and **H**, the combination of DNA and H_2O_2.

Journal Pre-proof

From a functional standpoint, the distorted octahedral geometry observed around the Cu(II) center is of particular interest. Coordination environments of this type, especially in Jahn–Teller active Cu(II) systems, are often linked to a certain degree of redox flexibility. In this context, such structural characteristics may be related to the DNA cleavage activity detected for compound (**1′**) under oxidative conditions, where Cu-centered redox processes are frequently involved. Although a detailed mechanistic analysis was not pursued in this study, the crystallographic features of

compound (**1**) offer a plausible structural framework to account for the nuclease-like behavior observed at the submicro-scale. Beyond simply defining the extended framework, the hydrogen-bonding network together with aromatic stacking interactions play a crucial role in shaping how the coordination polymer is presented at the molecular surface. These supramolecular characteristics can modulate the way the material engages with biological substrates, particularly nucleic acids, and may therefore provide an indirect contribution to the DNA-cleavage activity observed for compound (**1′**).

Compound (**1′**) exhibited moderate antibacterial activity against both Gram-positive (*B. subtilis*, *S. aureus*) and Gram-negative (*E. coli*, *P. aeruginosa*) bacteria, with inhibition zones of 6.00–9.26 mm, MIC values of 25–125 µg/mL, and MBC values of 1–25 µg/mL. The MBC/MIC ratios below 4 for all tested strains confirm bactericidal activity. The highest activity was observed against *S. aureus* (MIC = 25 µg/mL), while the lowest was against *E. coli* (MIC = 125 µg/mL). Antifungal activity against *C. albicans* was negligible (inhibition zones of 6–7 mm).

The antimicrobial activity of compound (**1′**) is attributed to multiple mechanisms. The Cu(II) center interacts with bacterial membranes through electrostatic interactions, causing membrane disruption and increased permeability. The 4,4'-bipyridine and 4-carboxybenzaldehyde ligands facilitate DNA binding through π–π stacking and intercalation between base pairs. The carboxylate group enhances cellular uptake, while the aldehyde moiety can form Schiff bases with amino groups of bacterial proteins, leading to protein inactivation.

Strikingly, compound (**1′**) exhibited strong DNA cleavage activity comparable to hydrogen peroxide (H_2O_2) in gel electrophoresis experiments, completely degrading DNA extracted from both *C. albicans* and *E. coli*. This broad-spectrum nuclease-like activity arises from copper-

mediated coordination to DNA phosphate groups and nucleobases, intercalation of aromatic ligands between base pairs, and oxidative damage to the deoxyribose backbone. The distorted octahedral geometry around the Cu(II) center, with its Jahn–Teller elongation, provides an accessible coordination site for DNA binding, while the aromatic ligands enhance intercalation through π–π stacking interactions.

The duality of strong DNA cleavage but moderate antibacterial activity suggests that limited cellular penetration, rather than lack of biochemical potency, is the primary factor restricting the overall antimicrobial efficacy. The dense 2D layered structure, lack of porosity, and bulky 4-carboxybenzaldehyde ligands likely hinder diffusion across bacterial membranes, particularly the outer membrane of Gram-negative bacteria. This interpretation is supported by the lower activity against Gram-negative strains compared to Gram-positive ones, consistent with the additional permeability barrier in Gram-negative organisms.

In the context of antimicrobial resistance, compound (**1′**) offers advantages through its multi-target mechanism simultaneously affecting DNA, proteins, and membrane integrity making it difficult for bacteria to develop resistance through single mutations. Its potent nuclease activity and bactericidal nature position it as a promising lead compound for further optimization. Future research should focus on enhancing cellular permeability through structural modifications such as introducing hydrophilic groups, reducing particle size, or designing more porous frameworks while preserving the strong DNA cleavage capability. These findings provide a foundation for the rational design of Cu(II)-based coordination polymers as next-generation antimicrobial agents to combat multidrug-resistant pathogens.

Journal Pre-proof

Compound (**1′**) showed moderate to low antibacterial activity against Gram-positive (*B. subtilis* and *S. aureus*) and Gram-negative (*E. coli* and *P. aeruginosa*) bacteria, with inhibition zones of 6.00–9.26 mm at 25–100 mg/mL and MIC values of 25–125 µg/mL. The highest activity was against *S. aureus* (MIC = 25 µg/mL). In contrast, the reference Cu(II) complexes (Kumar, Atria, Wang) were not evaluated for antibacterial activity in their respective studies, though similar complexes are known to exhibit moderate to good activity [49-51]. The relatively low activity of compound (**1′**) is attributed to its dense 2D structure, bulky ligands, and limited surface area, which restrict cellular penetration. However, compound (**1′**) exhibited strong DNA cleavage activity comparable to H_2O_2, indicating significant intrinsic nuclease-like potential, suggesting that its low antibacterial activity is due to poor cellular uptake rather than lack of biochemical reactivity **(**Table S6).

4. Conclusion

In this study, a new 2D Cu(II) coordination polymer was synthesized as bulk single crystals and as submicro-particles via ultrasound. SCXRD revealed a distorted octahedral Cu(II) geometry, while Hirshfeld analysis highlighted hydrogen bonding and π–π stacking as key stabilizing forces. The sonochemically prepared material exhibited plate-like morphology with narrow size distribution. Biological evaluations showed moderate, concentration-dependent antibacterial activity against both Gram-positive and Gram-negative bacteria, though lower than standard antibiotics. Notably, compound (**1′)** displayed strong DNA cleavage under oxidative conditions, indicating significant nuclease-like potential linked to its Cu(II) coordination environment. These findings establish a foundation for designing copper-based coordination polymers with tunable biological performance.

Journal Pre-proof

Journal Pre-proof

CRediT authorship contribution statement

M. A., Methodology, Data curation, Investigation, Writing-original draft preparation, **Kh. M.**, Supervisor, Conceptualization, Writing-original draft and review and editing preparation, **P. H.,** Supervisor, Writing-review and editing, **J. J**., Writing-review and editing and Software, **C. D. Z. Y.,** Software, **R. N.,** Methodology, Data curation.

Declaration of Competing Interests

The authors declare that they have no known competing financial interests or personal relationships that could have appeared to influence the work reported in this paper. All authors confirm that they have nothing to declare.

Journal Pre-proof

Acknowledgment

This work was supported by Persian Gulf University, Iran

Funding

No funding was received.

Supplementary data

The structural crystallographic data described in the current study have been preserved by the Cambridge Crystallographic Data Centre under the number CCDC-2353163. These details are available for free at http://www.ccdc.cam.ac.uk/conts/retrieving.html or from the Cambridge

Crystallographic Data Centre, 12 Union Road, Cambridge CB2 1EZ, UK; fax: +44-1223-336-033; or e-mail: deposit@ccdc.cam.ac.uk.

References

[1] G. Chakraborty, I. H. Park, R. Medishetty, J. J. Vittal, Two-dimensional metal-organic framework materials: synthesis, structures, properties and applications, Chem. Rev. 121 (2021) 3751-3891. https://doi.org/10.1021/acs.chemrev.0c01049.

[2] M. H. Kumar, M. S. Kumar, J. Y. Lin, S. K. Batabyal, Bio-polymer pectin as morphological modifier for polyaniline: Stability enhancement for energy storage applications, Mater. Sci. Semiconductor Process. 186 (2025) 109022. https://doi.org/10.1016/j.mssp.2024.109022.

[3] A. Dhakshinamoorthy, A. M. Asiri, H. Garcia, 2D metal-organic frameworks as multifunctional materials in heterogeneous catalysis and electro/photocatalysis, Adv. Mater. 31 (2019) 1900617. https://doi.org/https://doi.org/10.1002/adma.201900617.

[4] A. Benrashid, D. Habibi, M. Beiranvand, M. M. Gilan,The L-proline modified Zr-based MOF (Basu-proline) catalyst for the one-pot synthesis of dihydropyrano[3,2-c_chromenes], Sci. Rep. 13 (2023) 17608. https://doi.org/10.1038/s41598-023-44774-4.

[5] J. Liu, et al. MOF-enabled confinement and related effects for chemical catalyst presentation and utilization, Chem. Soc. Rev. 51 (2022) 1045-1097. https://doi.org/10.1039/D1CS00968K.

[6] H. Alamgholiloo, S. Zhang, A. Ahadi, S. Rostamnia, R. Banaei, Z. Li, X. Liu, M. Shokouhimehr, Synthesis of bimetallic 4-PySI-Pd@ Cu (BDC) via open metal site Cu-MOF:

effect of metal and support of Pd@ Cu-MOFs in H2 generation from formic acid, Mol. Catal. 467 (2019) 30. https://doi.org/10.1016/j.mcat.2019.01.031.

[7] Y. H. Lee, Y. Atoini, S. Kusumoto, S. Hayami, Y. Kim, J. Harrowfield and P. Thuéry,. Protic oligozwitterions as a means of introducing strong hydrogen bonding interactions in uranyl ion coordination polymers, Anorg. Allgem. Chem. 651(3) (2025) e20240021. http://doi.org/10.1002/zaac.202400217.

[8] N. Hoot et al. Synthesis of pyridone derivatives using 2D rod like bifunctional Fe based MOF and CuO nanocomposites as a novel heterogeneous catalyst, Sci. Rep. 13 (2023**)** 15753. https://doi.org/10.1038/s41598-023-43045-6.

[9] D. Majumdar, A, Frontera, S. Roy, D. Sutradhar, Experimental and theoretical survey of Intramolecular Spodium Bonds/o/ π-Holes and noncovalent interactions in Trinuclear Zn (II)-Salen type complex with OCN^- ions: a holistic view in crystal engineering, ACS Omega. 9 (2024) 1786−1797. https://doi.org/10.1021/acsomega.3c08422.

[10] S. Hazra, D. Majumdar, A, Frontera, S. Roy, B. Gassoumi, H. Ghalla, S. Dalai, On the significant importance of Hg..• Cl spodium bonding/o/n-hole/noncovalent interactions and nanoelectronic/conductivity applications in mercury complexes: insights from DFT spectrum, Cryst. Growth Des. 24(17) (2024**)** 7246–7261. https://pubs.acs.org/doi/10.1021/acs.cgd.4c00893.

[11] J. E. Cun , X. Fan , Q. Pan , W. Gao , K. Luo , B. He, Y. Pu, Copper-based metal-organicframeworks for biomedical applications, Adv. Colloid Interface Sci. 305 (2022) 102686. https://doi.org/10.1016/j.cis.2022.102686.

Journal Pre-proof

[12] S. Bonthula, S. R. Bonthula, R. Pothu, R. K. Srivastava, R, Boddula, A. B. Radwan, N. Al-Qahtani, Recent advances in copper-based materials for sustainable environmental applications, Sustain. Chem. 4(3) (2023) 246-271. https://doi.org/10.3390/suschem4030019.

[13] F. Vakil, M. Shahid, Sh. A. Siddiqui, I. Ahmad, S. Fatima, A. Tariq, A three-dimensional copper(II) MOF with sql topology: Design, crystal structure, supramolecular features, and antimicrobial activity, J. Mol. Struct. 1350 (2026) 144072. https://doi.org/10.1016/j.molstruc.2025.144072

[14] M. Ibrahim, Gh. A. Mahmoud, A. A. M. Ali, D. M. Fouad, Sonochemical synthesis of Cu(II) coordination polymer: Structural characterization and antibacterial activities against human pathogenic bacteria, Inorg. Chem. Commun, 168 (2024) 112951. https://doi.org/10.1016/j.inoche.2024.112951

[15] J. Zhao, T. Xu, J. Sun, H. Yuan, M. Hou, Zh. Li, J. Wang, Zh. Liang, Multifunctional nanozyme-reinforced copper-coordination polymer nanoparticles for drug-resistance bacteria extinction and diabetic wound healing, Biomater. Res. (2023) 2788. https://doi.org/10.1186/s40824-023-00429-z

[16] B. Y. Yua, H. Yina, Z. Abulikemua, F. T. Zhang, Y. Jiab, Z. X. Zouc, Y. Chen, Antimicrobial activities of three Cu-based coordination polymers, Polyhedron, 261 (2024) 117082. https://doi.org/10.1016/j.poly.2024.117082

[17] F. U. Xizhe, B. Tarun, C. Giancarlo, L. Zisheng, Sono-physical and sono-chemical effects of ultrasound: Primary applications in extraction and freezing operations and influence on food components, Ultrason. Sonochem. 60 (2020) 104726. https://doi.org/10.1016/j.ultsonch.2019.104726.

[18] H. Huang, Y. Zheng, M. Chang, J. Song, L. Xia, C. Wu, W. Jia, H. Ren, W. Feng, Y. Chen, Ultrasound-based micro-/nanosystems for biomedical applications, Chem. Rev. 124 (2024) 8307-8472. doi:10.1021/acs.chemrev.4c00009.

[19] M. J. Soltanian Fard, H. Naraghi, Synthesis and structural characterization of a new 2-D lead (II) supramolecule: A new precursor for preparation PbO nanoparticles via thermal decomposition, J. Mol. Struct. 1035 (2013) 236-239. https://doi.org/10.1016/j.molstruc.2012.10.043.

[20] H. N. Kim, K. S. Suslick, The effects of ultrasound on crystals: Sonocrystallization and sonofragmentation, Crystals. 8(7) (2018) 280. https://doi.org/10.3390/cryst8070280.

[21] M. C. V. Sosa, I. M. S. Gaona, C. A. P. Vargas , R. J. Rincón, D. L. Pérez, Evaluation of ultrasonic energy and temperature on the structural, morphological, and magnetic properties of Fe_30_4 nanoparticles, Solid State Sci. 162 (2025) 107880. https://doi.org/10.1016/j.solidstatesciences.2025.107880.

[22] K. M. Ismail, F. B. Rashidi, S. S. Hassan, Ultrasonic synthesis, characterization, DFT and molecular docking of a biocompatible Zn-based MOF as a potential antimicrobial, anti-inflammatory and antitumor agent, Sci. Rep. 14 (2024) 21989. https://doi.org/10.1038/s41598-024-71609-7.

[23] S. He, S. Zhong, Q. Meng, Y. Fang, Y. Dou, Y. Gao, X. Cui, Sonochemical preparation of folate-decorated reductive-responsive carboxymethylcellulose-based nanocapsules for targeted drug delivery, Carbohydr. Polym. 266 (2021) 118174, doi: 10.1016/j.carbpol.2021.118174.

Journal Pre-proof

Journal Pre-proof

[24] S. Shabana, R. Prasansha, I. Kalinina, I. Potoroko, U. Bagale, S. H. Shirish, Ultrasound assisted acid hydrolyzed structure modification and loading of antioxidants on potato starch nanoparticles, Ultrason. Sonochem. 51 (2019) 444-450, doi:10.1016/j.ultsonch.2018.07.023.

[25] J. J. Hinman, K. S. Suslick, Nanostructured materials synthesis using ultrasound, Springer. Cham. (2017) 59–94. doi:10.1007/978-3-319-54271-3_3.

[26] H. Sun et al, Sonochemical synthesis of battery-type ZnCo204 electrode material with huge specific surface area for advanced hybrid supercapacitors, J Energy Storage. 76 (2024). https://doi.org/10.1016/j.est.2023.109780.

[27] J. Lee, K. Yasui, M. Ashokkumar, S. E. Kentish, Quantification of cavitation activity by sonoluminescence to study the sonocrystallization process under different ultrasound parameters, Cryst. Growth Des. 18 (2018) 5108-5115. doi:10.1021/acs.cgd.8b00547.

[28] N. Zare, A. Zabardasti, A. Mohammadi, F. Azarbani, A. Kakanejadifard, Sonochemical synthesis, characterization, biological applications, and DFT study of new nano-sized manganese complex of azomethine derivative of diaminomaleonitrile, J. Iran. Chem. Soc. 16 (2019) 1501-1516. doi:10.1007/s13738-019-01626-1.

[29] P. Hayati, A. Rezvani, A. Morsali, P. Retailleau, R. Centore, Survey of temperature, reaction time and ultrasound irradiation power on sonochemical synthesis of two new nanostructured lead (II) coordination supramolecule compounds, Ultrason. Sonochem. 35 (2017) 81-91. https://doi.org/10.1016/j.ultsonch.2016.09.005.

[30] M. J. Soltanain Fard, P. Hayati, A. Firoozadeh, J. Janczak, Ultrasonic synthesis of two new zinc (II) bipyridine coordination nano-particles polymers: new precursors for preparation of

zinc (II) oxide nano-particles, Ultrason. Sonochem. 35 (2017) 502-513. https://doi.org/10.1016/j.ultsonch.2016.11.009.

[31] Z. Y. Qian, V.A. Blatov, T. R. Zheng, C. H. Yang, L. L. Qian, K. Li, B. L. Li, B. Wu, A luminescent zinc (II) coordination polymer with unusual (3, 4, 4)-coordinated self-catenated 3D network for selective detection of nitroaromatics and ferric and chromate ions: a versatile luminescent sensor, Dalton Trans. 47(17) (2018) 6189-6198. https://doi.org/10.1039/C7DT04682K.

[32] M. Yue, Y. Ni, F. Guo, N. Xiang, Flowerlike copper (II)-based coordination polymers particles: Rapid room-temperature fabrication, influencing factors, and transformation toward CuO microstructures with good catalytic activity for the reduction of 4-nitrophenol, Crys. Growth Des. 15(5) (2015) 2243-2252. https://doi.org/10.1021/acs.cgd.5b00003.

[33] K. Zhao, J. Wu, X. Li, Zh. Li, Y. Chen, Advances of ultrasonic scaling removal technology and heat transfer enhancement technology, Chem. Bio. Eng. Rev. 2 (2021) 134–144, doi:10.1002/cben.202000020.

[34] D. Meroni, R. Djellabi, M. Ashokkumar, C. L. Bianchi, D. C. Boffito, sonoprocessing: from concepts to large-scale reactors, Chem. Rev. 122 (2022) 3219–3258, https://doi.org/10.1021/acs.chemrev.1c00438.

[35] T. Daisuke, A. Henke, K. Albrecht, M. Moeller, K. Nakagawa, S. Kitagawa, J. Groll, Rapid preparation of flexible porous coordination polymer nanocrystals with accelerated guest adsorption kinetics, Nat. Chem. 2 (5) (2010) 410-416. https://doi.org/10.1038/nchem.627.

[36] L. Hashemi, A. Morsali, Microwave assisted synthesis of a new lead (II) porous three-dimensional coordination polymer: study of nanostructured size effect on high iodide

Journal Pre-proof

adsorption affinity, Cryst. Eng. Comm. 14(3) (2012) 779-781. https://doi.org/10.1039/C2CE06133C.

[37] A. O. Pilar, G. Givaja, P. J. S. Miguel, O. Castillo, F. Zamora, Microwave assisted hydrothermal synthesis of a novel CuI-sulfate-pyrazine MOF, Inorg. Chem. Commun. 10(8) (2007) 921-924. https://doi.org/10.1016/j.inoche.2007.04.024.

[38] R. Nidhi, S. Randhir, K. Praveen, Imidazole and derivatives drugs synthesis: A review, Curr. Org. Synth. 20(6) (2023) 630-662. https://doi.org/10.2174/1570179420666221118100525.

[39] Y. J. Jang, J. H. Han, K. S. Min, Ferromagnetic chloro-bridged copper(II) coordination polymer: Synthesis, structure, magnetism, and DNA cleavage effects, J. Mol. Struct. 1271 (2023) 134136. 10.1016/j.molstruc.2022.134136

[40] V. Psycharis, D. Dermitzaki, C. P. Raptopoulou, The use of Hirshfeld surface analysis tools to study the intermolecular interactions in single molecule magnets, Crystals, 11(10) (2021) 1246. https://doi.org/10.3390/cryst11101246.

[41] A. Ouertani, C. Mollet, Y. Boughanmi, H. de Pomyers, A. Mosbah, H.-I. Ouzari, A. Cherif, D. Gigmes, M. Maresca, K. Mabrouk, Screening of antimicrobial activity in venom: Exploring key parameters, Toxicon. 251 (2024) 108135. https://doi.org/10.1016/j.toxicon.2024.108135.

[42] D. Majumdar, J. E. Philip, B. Tüzün, S. Roy, Synthesis, characterization, crystallographic aspects, Fukui function, and photodynamic antifungal chemotherapy investigation of Cd (II) tricyanomethanide coordination polymer: insights from DFT, Inorg. Chem. Commun. 155 (2023) 111057. https://doi.org/10.1016/j.inoche.2023.111057.

[43] P. k. Pandey, B. Kumar, A. Kumari, S. Kumari, Assessment of antifungal activity of henna (Lawsonia inermis) leaves extract (aqueous) with commercial antifungal drug by disc

diffusion method against Canine Fungal Dermatitis, J. Adv. Biol. Biotechnol. 28(5) (2025) 394-398. Doi:10.9734/jabb/2025/v28i52301.

[44] C. Rodríguez-Melcón, C. Alonso-Calleja, C. García-Fernández, J. Carballo, R. Capita, Minimum inhibitory concentration (MIC) and minimum bactericidal concentration (MBC) for twelve antimicrobials (biocides and antibiotics) in eight strains of Listeria monocytogenes, Biology (Basel). 11(1) (2021) 46. https://doi.org/10.3390/biology11010046.

[45] Z. Akbari, M. Montazerozohori, S. J. Hoseini, R. Naghiha, Ultrasonic assisted preparation of some new zinc complexes of a new tetradentate Schiff base ligand: thermal analyses data, antimicrobial and DNA cleavage potential, J. Phys. Org. Chem. 34(5) (2021) e4180. https://doi.org/10.1002/poc.4180.

[46] M. Hamidian, A. Salehi, R. Naghiha, M. Movahhedi Dehnavi, H. Mohammadi, M. Nejad Mirfathi, M. Mojarab-Mahboubkar, R. Azizi, Biological activity of essential oils from Ferulago angulata and Ferula assa-foetida against food-related microorganisms (antimicrobial) and Ephestia kuehniella as a storage pest (insecticidal); an *in vitro* and in silico study, Fitoterapia, 175 (2024) 105937. https://doi.org/10.1016/j.fitote.2024.105937.

[47] M. A. Vershinin, S. A. Adonin, Crystal structures of $CoCl_2$ $6H_2O$ reaction products with 2-methylpyridine and 2,6-dimethylpyridine, J. Struct. Chem. 62(1) (2021) 90-94. https://doi.org/10.1134/S0022476621010108.

[48] H. Phetmung, S. Wongsawat, Ch. Pakawatchai, D. J. Harding, Microwave synthesis, spectroscopy, thermal analysis and crystal structure of an one-dimensional polymeric {[Cu(4,4′-bipy)$(H_2O)_3(SO_4)$] $2H_2O$}n complex, Inorg. Chim. Acta. 362 (2009) 2435–2439. doi:10.1016/j.ica.2008.10.038.

[49] Y. Wang, R. Cao, W. Bi, X. Li, D. Yuan, D. Sun, Four novel porous frameworks constructed by formate ligand, Microporous Mesoporous Mater. 91 (2006) 215–220. doi:10.1016/j.micromeso.2005.11.046.

[50] D. Kumar, I. P. S. Kapoor, G. Singh, R. Fröhlich, Preparation, characterization, and kinetics of thermolysis of nickel and copper nitrate complexes with 2,2′-bipyridine ligand, Thermochim. Acta. 545 (2012) 67–74. http://dx.doi.org/10.1016/j.tca.2012.06.032.

[51] A, M, Atria, P. Cortés, M. T. Garland, R. Baggio, [Cu(2-Me-imidH)$_4$Cl]Cl: a conflict between high symmetry and packing efficiency, Acta. Cryst. (2003) E59, m1075-m1077. DOI: 10.1107/S1600536803024553.

[52] D. Hagrman, R. P. Hammond, R. Haushalter, J, Zubieta, Organic/inorganic composite materials: Hydrothermal syntheses and structures of the one-, two-, and three-dimensional copper(II) sulfate−organodiamine phases [Cu(H_2O)$_3$(4,4‘-bipyridine)(SO_4)]·2H_2O, [Cu(bpe)$_2$][Cu(bpe)(H_2O)$_2$(SO_4)$_2$]·2H_2O, and [Cu(bpe)(H_2O)(SO_4)] (bpe = trans-1,2-bis(4-pyridyl)ethylene), Chem. Mater. 10 (1998) 2091–2100. https://doi.org/10.1021/cm9707566.

[53] M. K. Mohammadi, R. Khoshnavazi, S. Geravand, M. Karimi, P. Retailleau, A. Masoudiasl, G. Mahmoudi, Synthesis, crystal structure and Hirshfeld surface analysis of a new OD nanostructured [{(Ar-Cl)tetra-azo-S}$_2$Hg] coordination supramolecular compound derived from phenyl isothiocyanate ligand, J. Coord. Chem. (2019) 1-12. https://doi.org/10.1080/00958972.2019.1613531.

[54] J. J. McKinnon, D. Jayatilaka, M. A. Spackman, Towards quantitative analysis of intermolecular interactions with Hirshfeld surfaces, Chem. Commun. (2007) 3814-3816. https://doi.org/10.1039/B704980C.

Journal Pre-proof

[55] O. Urgut, I. Ozturk, C. Banti, N. Kourkoumelis, M. Manoli, A. Tasiopoulos, S. Hadjikakou, New antimony (III) halide complexes with dithiocarbamate ligands derived from thiuram degradation: The effect of the molecule's close contacts on in vitro cytotoxic activity, Mater. Sci. Engin. C. 58 (2016) 396-408. https://doi.org/10.1016/j.msec.2015.08.030.

[56] B. K. Kim, Y. L. Jo, J. J. Shim, Preparation and antibacterial activity of silver nanoparticles-decorated graphene composites, J. Supercrit. Fluids. 72 (2012) 28-35. https://doi.org/10.1016/j.supflu.2012.08.005.

[57] E. Romano, P. G. Cataldo, M. A. Iramain, M. V. Castillo, M. E. Manzur, S. Antonia Brandán, Identification of cholesterol in different media by using the FT-IR, FT-Raman and UV-visible spectra combined with DFT calculations, J. Mol. Liquids. 403 (2024) 124879. https://doi.org/10.1016/j.molliq.2024.124879.

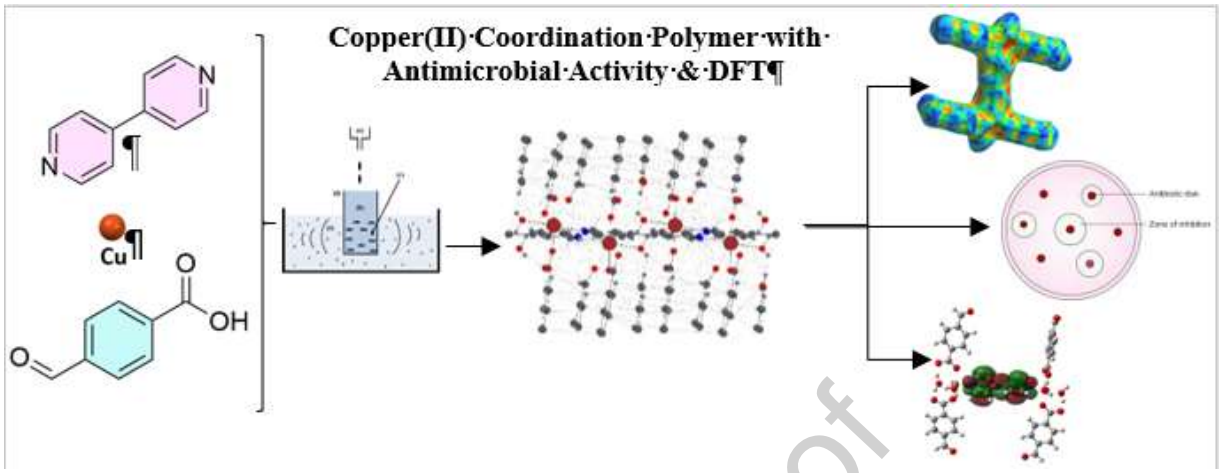
[58] M. J. Frisch, et al.; Gaussian 03, Revision B.01, Gaussian Inc., Pittsburgh PA, 2003.

[59] K. Ngece, V. Khwaza, A.M. Paca, B. A. Aderibigbe. The antimicrobial efficacy of copper complexes: A review. Antibiotics (Basel), 2025 May 16, 14(5) (2025) 516. doi:10.3390/antibiotics14050516.

[60] H. V. Tolomeu, C. A. M. Fraga, Imidazole: Synthesis, functionalization and physicochemical properties of a privileged structure in medicinal chemistry, Molecules, 28(2) (2023) 838. https://doi.org/10.3390/molecules28020838.

[61] A. Hamdi, W. Daoudi, M. Aaddouz, M. Azzouzi, H. Amhamdi, A. Elyoussfi, A. E. Aatiaoui, D. K. Verma, M. Abboud, M. H. Ahari, Various synthesis and biological evaluation of some tri -tetra-substituted imidazoles derivatives: A review, Heliyon. 10(10) (2024) e31253. https://doi.org/10.1016/j.heliyon.2024.e31253.

Graphical abstract



Declaration of interests

☒ The authors declare that they have no known competing financial interests or personal relationships that could have appeared to influence the work reported in this paper.

☐ The authors declare the following financial interests/personal relationships which may be considered as potential competing interests:

Journal Pre-proof